Article

Cancer Cell

Unbiased Combinatorial Screening Identifies a Bispecific IgG1 that Potently Inhibits HER3 Signaling via HER2-Guided Ligand Blockade

Graphical Abstract

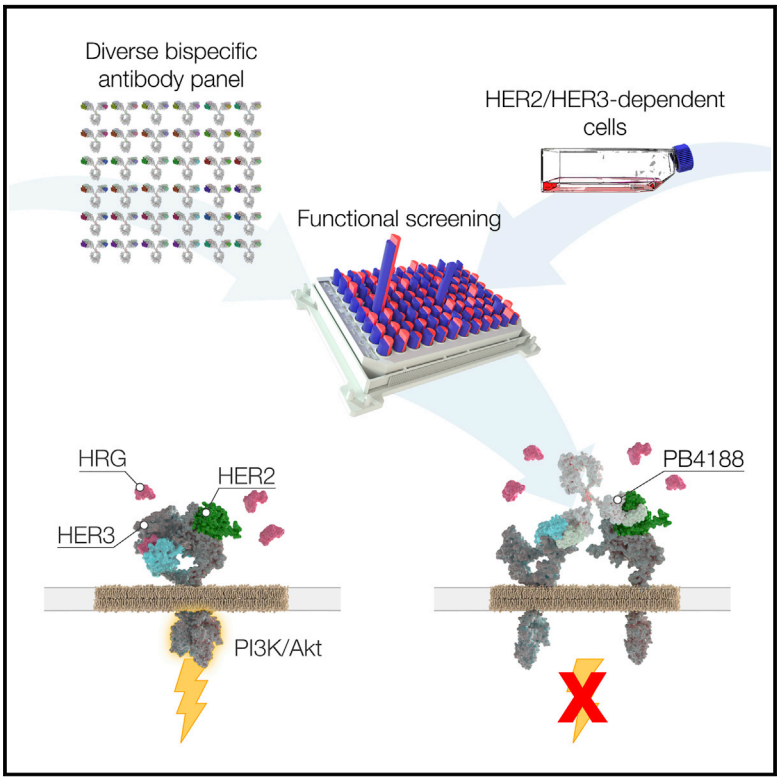

Authors

Cecile A.W. Geuijen, Camilla De Nardis, David Maussang, ..., John de Kruif, Piet Gros, Mark Throsby

Correspondence

m.throsby@merus.nl

In Brief

Geuijen et al. identify a bispecific IgG1 antibody against HER2 and HER3 using a phenotypic combinatorial screening approach. This antibody potently inhibits the heregulin/HER3 pathway and downstream PI3K/Akt signaling via a "dock & block" mechanism in tumor models resistant to agents targeting HER2.

Highlights

- Unbiased phenotypic screening identifies bispecific antibody with unique properties
- Therapeutic agent that potently and specifically blocks the HRG/HER3 pathway
- Dock and block mechanism of action dependent on bispecific format

Geuijen et al., 2018, Cancer Cell *33*, 922–936
May 14, 2018
https://doi.org/10.1016/j.ccell.2018.04.003

CellPress

CellPress

Cancer Cell
Article

Unbiased Combinatorial Screening Identifies a Bispecific IgG1 that Potently Inhibits HER3 Signaling via HER2-Guided Ligand Blockade

Cecile A.W. Geuijen,[1] Camilla De Nardis,[2] David Maussang,[1] Eric Rovers,[1] Tristan Gallenne,[1] Linda J.A. Hendriks,[1] Therese Visser,[1] Roy Nijhuis,[1] Ton Logtenberg,[1] John de Kruif,[1] Piet Gros,[2] and Mark Throsby[1,3,*]

[1]Merus NV, 3584 Utrecht, the Netherlands

[2]Crystal and Structural Chemistry, Bijvoet Center for Biomolecular Research, Department of Chemistry, Faculty of Science, Utrecht University, 3584 Utrecht, the Netherlands

[3]Lead contact

*Correspondence: m.throsby@merus.nl

https://doi.org/10.1016/j.ccell.2018.04.003

SUMMARY

HER2-driven cancers require phosphatidylinositide-3 kinase (PI3K)/Akt signaling through HER3 to promote tumor growth and survival. The therapeutic benefit of HER2-targeting agents, which depend on PI3K/Akt inhibition, can be overcome by hyperactivation of the heregulin (HRG)/HER3 pathway. Here we describe an unbiased phenotypic combinatorial screening approach to identify a bispecific immunoglobulin G1 (IgG1) antibody against HER2 and HER3. In tumor models resistant to HER2-targeting agents, the bispecific IgG1 potently inhibits the HRG/HER3 pathway and downstream PI3K/Akt signaling via a "dock & block" mechanism. This bispecific IgG1 is a potentially effective therapy for breast cancer and other tumors with hyperactivated HRG/HER3 signaling.

INTRODUCTION

Human epidermal growth factor receptor 3 (HER3) is a member of the ErbB family of receptor tyrosine kinases, which regulate the proliferation and survival of epithelial cells (Yarden and Pines, 2012). Unlike other ErbB family members such as epidermal growth factor receptor (EGFR) and HER2 (encoded by *ERBB2*), HER3 (encoded by *ERBB3*) lacks intrinsic kinase activity. However, HER3 is a potent activator of the phosphatidylinositide-3 kinase (PI3K)/Akt survival pathway, making it a key dimerization partner for other ErbB family members. HER3 is also essential for the survival of HER2-dependent tumors (Holbro et al., 2003). HER2 requires dimerization with HER3 to engage and activate the PI3K/Akt growth and survival pathway, which is essential for tumor expansion (Lee-Hoeflich et al., 2008). HER2/HER3 dimers can form in the absence of HER3 ligand heregulin (HRG), but their abundance, stability and signaling output is increased in the presence of HRG (Junttila et al., 2009).

Targeted therapy of HER2-dependent tumors depends on kinase inhibition. These tumors can become insensitive to kinase inhibition through upregulation of the HRG/HER3 pathway (Sergina et al., 2007; Wilson et al., 2012). Studies have shown that persistent and complete inhibition of HER3 and its output to PI3K/Akt is likely needed for the optimal anti-tumor effect of therapeutic inhibitors of HER2 (Garrett et al., 2013). Hyperactivation of the HRG/HER3 pathway in tumors can result from translocation of *HRG* (Fernandez-Cuesta et al., 2014), HRG, and/or HER3 transcriptional upregulation in response to therapy (Chakrabarty et al., 2012; Chandarlapaty et al., 2011; Hegde et al., 2013; Wilson et al., 2011), or HRG release from surrounding stroma (Capparelli et al., 2015; Saunus et al., 2015; Shames et al., 2013). Analysis of publically available gene expression databases shows that HRG overexpression is detectable in many

Significance

In patients with HER2-positive tumors, activation of the HRG/HER3 tumor-signaling pathway is thought to worsen prognosis. Here we demonstrate highly selective and potent pharmacological inhibition of this pathway. We produced >500 anti-HER2xHER3 bispecific antibodies and screened them in functional assays. From this screen, we identified PB4188, whose therapeutic properties were superior to those of monoclonal antibodies against the same targets, tested as single agents or in combination. The unbiased screening approach used here is broadly applicable to the discovery of therapeutic bispecific antibodies in oncology and other therapeutic areas. MCLA-128, the development candidate of PB4188, is under clinical evaluation in various solid tumor indications.

tumor samples from patients. High levels of HRG—and also of HER3—have been associated with poor outcome in several tumor types including breast cancer (BC), ovarian cancer (OC), squamous cell carcinoma of the head and neck, and non-small-cell lung carcinoma (NSCLC) (Liu et al., 2016; Muller-Tidow et al., 2005; Ocana et al., 2013; Shames et al., 2013). The observation in HER2-overexpressing BC cells *in vitro* that autocrine HRG expression and secretion and/or HER3 upregulation can be induced by treatment with trastuzumab (Gijsen et al., 2010; Narayan et al., 2009; Ritter et al., 2007) may explain why some BC patients progress on trastuzumab (Nonagase et al., 2016). Similarly, HRG autocrine feedback was shown to be an important driver of resistance to platinum therapy and may be operational in >25% of advanced OC patients (Pradeep et al., 2014; Sheng et al., 2010). Finally, high levels of HER3 expression and activation of the HRG/HER3 pathway have been reported in estrogen receptor (ER)-positive luminal BC in response to anti-endocrine therapy (Morrison et al., 2013).

Current therapeutic approaches to suppress activation of the HRG/HER3 pathway have focused on inhibiting intracellular kinase activity, preventing HER2 dimerization, or inhibiting ligand binding to HER3 itself. Monoclonal antibodies (mAbs) that target HER3 offer the most direct approach to interfere with HRG/HER3 pathway activation, and several are under development (Berlin et al., 2011; Garner et al., 2013; Lee et al., 2015; Mirschberger et al., 2013; Schoeberl et al., 2010). Despite anti-tumor activity seen in some patient subgroups when HER3 mAbs are combined with other drugs, these findings have not translated into meaningful clinical benefit when assessed in larger trials (Liu et al., 2016; Paz-Arez et al., 2017; Reynolds et al., 2014; Sequist et al., 2014; Yonesaka et al., 2017). Other therapeutic agents that may be capable of inhibiting HRG/HER3 pathway activation more efficiently include bispecific antibodies (bAbs). Full-length bAbs not only contain two different arms that enable them to target two antigens simultaneously, they also have favorable drug-like properties such as long half-life and the potential for enhanced functionality (De Nardis et al., 2017; Kontermann and Brinkmann, 2015). To address the shortcomings of current therapeutic strategies, we undertook an unbiased screening approach to identify a full-length bAb targeting the extracellular domain (ECD) of HER2 and HER3 that specifically and potently blocks HRG-driven signaling of the HER2/HER3 heterodimer.

RESULTS

Unbiased Screening Leads to Identification of Potent Tumor Growth-Inhibiting bAbs

To develop a therapeutic agent that effectively and specifically inhibits ligand-dependent activation of the HER2/HER3 dimer, we screened more than 500 bAbs targeting both HER2 and HER3 (Figure S1). The HER2 and HER3 common light chain (cLC) antigen-binding fragments (Fabs) were selected based on their epitope and sequence diversity to combine in the bAb format. This allowed us to screen a highly diverse bAb panel for functional activity without making any assumptions on the optimal Fab affinity or binding site based on modeling or mAb activity.

To generate the required diversity for this unbiased combinatorial screening approach, C57/BL6 mice were immunized by cell, protein, or DNA vaccination, and heterologous prime boost methods. Phage libraries were constructed using variable heavy chain (VH) genes isolated from the immune tissues of these animals, combined with a human cLC. Standard phage-display selection methods were applied to isolate a panel of 180 unique cLC Fabs based on heavy chain complementary-determining region 3 (HCDR3) sequence and VH germline gene usage. The Fab panel was then reformatted as human immunoglobulin G1 (IgG1) and characterized based on domain specificity. The HER2 panel was grouped into seven distinct epitope "bins" covering all HER2 domains (Table S1). Antibodies in the HER3 panel could not be binned based on domain specificity, probably due to the high sequence homology between rat and human HER3. These experiments did, however, result in binning of the HER3 panel into at least seven distinct groups based on different staining patterns and on HRG-neutralizing activity in an MCF-7 cell proliferation assay (Table S2).

The initial functional screening was performed with full-length HER2xHER3 bAbs (Figure 1A) generated using a mutated IgG1 Fc variant region known as DEKK, which drives efficient heterodimerization of the antibody heavy chains (De Nardis et al., 2017). Combinations of 22 HER2 and 32 HER3 cLC Fabs (Table S3) were selected to maximize bAb panel diversity based on the binning and ranking described above (Figure 1B). BxPC-3 cells, selected based on balanced HER2 and HER3 expression levels, were stimulated with exogenous HRG in starvation medium rendering the cells dependent on ligand for growth. All bAbs were tested at 10 and 1 μg/mL concentrations in the presence of HRG (HRG dependent) or absence of HRG (HRG independent) and compared with trastuzumab activity.

After the primary functional screen, the panel size was increased by including more bAbs with HER2 domain I binding Fabs as these bAbs showed the highest proliferation inhibition activity. This resulted in a total of 545 bAbs that were screened for proliferation inhibition in the BxPC-3 assay (n = 2). One hundred and ninety-two bAbs inhibited HRG-independent and 236 bAbs inhibited HRG-dependent proliferation; 82 were significantly more potent than trastuzumab in one or both assay settings. Validation screening with the most active HER2/HER3 arms in the BxPC-3 assay resulted in a selection of 40 bAbs that were reproduced for further functional screening (Figure 1C).

This panel of bAbs were titrated for growth-inhibiting activity on MCF-7 cells at submaximal HRG-driven growth conditions (0.125 nM) to increase assay sensitivity. A number of HER2 and HER3 mAbs as well as the bispecific construct MM-111 were produced (based on patent literature, marked with an asterisk) as controls to provide a benchmark for activity in functional assays (Figures S2A–S2E). In the MCF-7 assay, titration of HER2 mAbs trastuzumab or pertuzumab* alone demonstrated significant and dose-dependent inhibition of growth, but they were less effective than the equimolar combination of the two mAbs or than the anti-HER3 mAb MM-121* (Figure 2A). Several bAbs showed significantly greater potency than the combination of trastuzumab plus pertuzumab* (T + P*) (Figure 2B). The activity of the nine best growth-inhibiting HER2xHER3 bAbs *in vitro* was confirmed *in vivo*, in a validated orthotopic BxPC-3 xenograft model (Figure S2F). Four bAbs (PB3710, PB3448, PB3441, and PB3566) demonstrated significantly greater inhibition of tumor

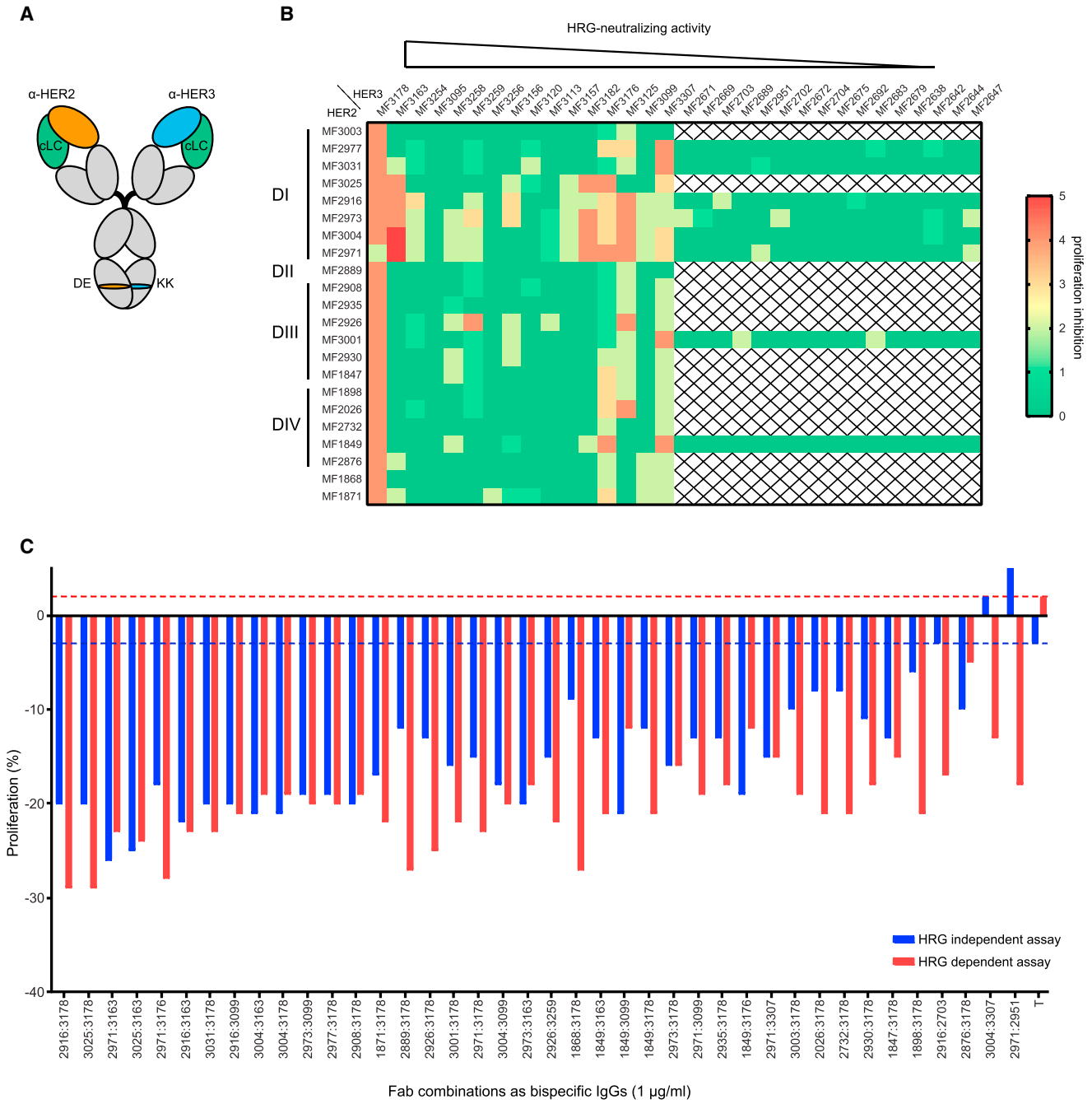

Figure 1. Screen of HER2xHER3 bAb Panel in BxPC-3 Cells

(A) Schematic representation of a full-length HER2xHER3 bispecific IgG obtained by combining a cLC with CH3 "DEKK" engineering (L351D/L368E and L351K/T366K) (De Nardis et al., 2017).

(B) Heatmap displaying the growth-inhibiting potential of bAbs composed of different HER2 (ranked on binning and domain binding) and HER3 (ranked on HRG-neutralizing activity) Fabs in BxPC-3 cells.

(C) Percentage change in proliferation inhibition activity in BxPC-3 cells of the selected 40 HER2xHER3 bAbs shown as HER2:HER3 Fab combinations, with or without HRG stimulation. Dotted lines represent activity of trastuzumab in the absence (blue) or presence (red) of HRG. See also Figure S1, Tables S1–S3.

growth relative to trastuzumab (Figures S2G and S2H). Clone PB3566, composed of Fab arms MF3004 and MF3178, was the most potent bAb both *in vitro* and *in vivo*. In the MCF-7 cell proliferation assay, PB3566 (half maximal effective concentration [EC_{50}] = 7.9 pM; n = 2) was 50-fold more potent than T + P* and 20-fold more potent than its parental bivalent HER3 mAb PG3178 (Table S4). The HER2 Fab of PB3566, which was derived from a mouse library, was humanized, and the sequence

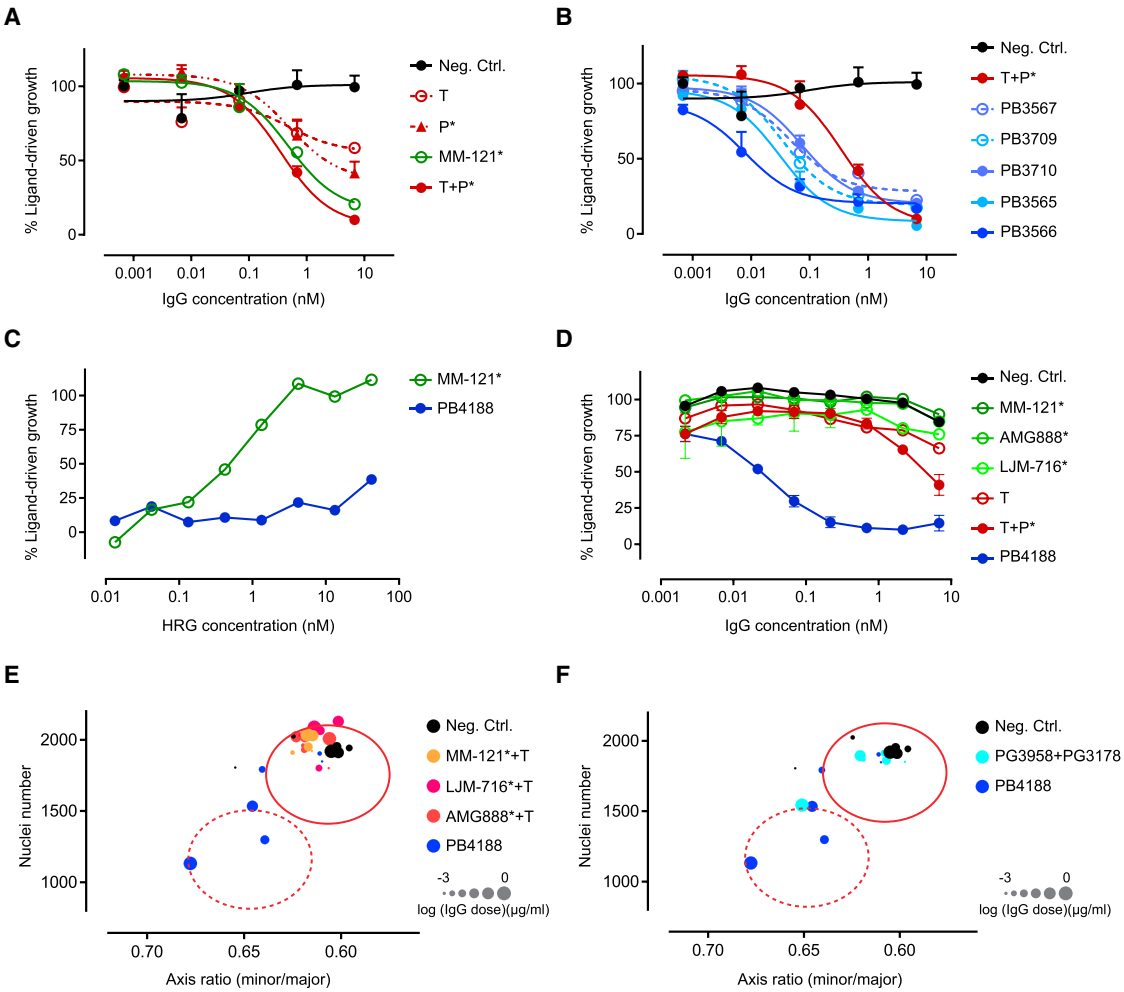

Figure 2. PB4188 Potently Inhibits HRG-Induced Proliferation

(A and B) Titration curves of anti-HER2 and anti-HER3 benchmark antibodies (A) and of bAbs (B) in MCF-7 cells supplemented with 0.125 nM HRG. bAbs shown in (B): PB3567 (MF2971xMF3178), PB3709 (MF3025xMF3178), PB3710 (MF2916xMF3178), PB3565 (MF2973xMF3178), and PB3566 (MF3004xMF3178).

(C) Growth of N87 cells treated with PB4188 or MM-121* (68 nM) and a titration of HRG.

(D) Growth of N87 cells stimulated with 12.5 nM HRG and a titration of the indicated antibodies.

(E and F) SKBR-3 cells were stimulated with 12.5 nM HRG, and PB4188 activity was compared with equimolar mixtures of trastuzumab and anti-HER3 mAbs (E) or equimolar mixtures of anti-HER2 and anti-HER3 PB4188 parental mAbs (F). Cell proliferation was measured by number of nuclei per well. Cell invasiveness phenotype was quantified by measuring cellular shape, dividing the shortest cell axis (minor) by the longest axis (major) of the SKBR-3 cell cluster. An axis ratio of 1 describes a sphere, while decreasing ratios are associated with more invasive structures. The red circles indicate the range of cell growth in the presence (full line) or absence (dashed line) of HRG without any antibody added. T, trastuzumab; P*, pertuzumab*; T + P*, equimolar combination of trastuzumab plus pertuzumab*. Data in (A, B, and D) are represented as means ± SEM. Data in (E and F) are represented as means of four data points. Data in (C) are from a representative experiment. Each experiment was done at least two independent times. See also Figures S2, S3, and Table S4.

was optimized to improve developability and manufacturability, resulting in the PB4188 variant bAb used in further experiments.

PB4188 Potently Inhibits Tumor Cell Growth under HRG Stress Conditions

Cancer cells can activate secondary signaling pathways resulting in resistance to receptor tyrosine kinase inhibition. In particular, high expression levels of growth factors such as HRG can bypass inhibition of primary oncogenic kinases (Sergina et al., 2007; Wilson et al., 2012). We performed titration experiments to establish the submaximal and supramaximal HRG concentrations for growth in the MCF-7 and N87 cell lines (Figure S2I). As previously reported for the tyrosine kinase inhibitor lapatinib (Wilson et al., 2012), the inhibitory activity of HER3 mAb MM-121* (68 nM, Figure 2C) was reduced in a dose-dependent manner as the HRG concentration increased beyond its EC_{90} value for growth stimulation (0.11 nM). In contrast, the HER2xHER3 bAb PB4188 at the same IgG concentration was able to suppress growth even at the highest ligand concentration tested. Under these supramaximal HRG or ligand "stress" conditions (>10 nM HRG), where HRG levels are ~100-fold greater than the EC_{90} for HRG-stimulated growth in N87 cells, PB4188 completely suppressed ligand-driven growth at IgG concentrations >1 nM (EC_{50} = 35 pM) (Figure 2D). In contrast, HER2- and

HER3-targeting mAbs failed to inhibit ligand-driven growth. Similarly, a previously described HER2xHER3 bispecific single chain fragment variable (scFv) antibody construct MM-111* (McDonagh et al., 2012) was unable to inhibit ligand-driven growth of N87 cells, although it was active at submaximal HRG-driven growth conditions (Figure S3A).

To confirm these results, we also carried out phenotypic profiling of additional *ERBB2*-amplified cell lines under HRG stress conditions, using high-content imaging to measure growth and invasive morphology, in the presence of PB4188 and control mAbs. PB4188 was capable of suppressing morphological parameters associated with HRG stimulation of SKBR-3 cells—both number of nuclei and membrane irregularity (Figure S3B)—in a dose-dependent manner (Figures 2E and 2F). However, we saw no such effect with the addition of mAbs targeting HER3 (Figure S3C), or equimolar mixtures of trastuzumab and anti-HER3 mAbs (Figure 2E), or equimolar mixtures of the HER2 and HER3 parental Fabs formatted as bivalent IgGs (Figure 2F). Phenotypic profiling using another *ERBB2*-amplified cell line (BT474) gave similar results (data not shown). Consistent with its ability to block cellular proliferation *in vitro*, PB4188 was significantly more potent than T + P* in blocking cell-cycle progression induced by both submaximal (Figure S3D) and supramaximal (Figure S3E) HRG stimulation, regardless of HER2 expression level. Collectively, these data demonstrate that the bAb PB4188 potently blocks HRG-driven proliferation of cancer cells. In *ERBB2*-amplified cell lines cultured under ligand stress conditions, PB4188 retained the ability to block HRG-driven proliferation unlike mAbs—individually or in combination—targeting HER2 and HER3.

PB4188 Selectively Inhibits Ligand-Mediated HER2/HER3 Heterodimerization and Downstream Signaling

All HER family members heterodimerize with each other to transduce intracellular signals that vary in both signal strength and the type of pathway activated (Yarden and Pines, 2012). The heterodimer specificity of PB4188 inhibition was investigated using β-galactosidase enzyme complementation technology in cell lines overexpressing pairs of HER family members that heterodimerize in response to ligand stimulation. In the group of HER2-containing dimers, pertuzumab* was capable of inhibiting EGF-induced heterodimerization of EGFR/HER2, as well as HRG-induced heterodimerization of HER2/HER4 and HER2/HER3 (Figures 3A–3C). PB4188 selectively inhibited formation of HER2/HER3 heterodimers, and was more potent than pertuzumab* or the HER3 mAb AMG888*. In the HRG-induced EGFR/HER3 dimerization assay, AMG888* was significantly more potent than PB4188 (Figure 3D). The less potent inhibitory activity of PB4188 on EGFR/HER3 dimers is presumably a consequence of monovalent HER3 interaction. As expected, pertuzumab* did not inhibit the formation of EGFR/HER3 dimers and, as shown previously, trastuzumab had a limited effect on HRG-induced HER2/HER3 heterodimerization (Junttila et al., 2009).

Given the known cardiovascular side effects of HER2-targeting agents, which are thought to result from HER2/HER4 signaling inhibition (Gassmann et al., 1995), we also tested PB4188 for toxicity on adult cardiomyocytes *in vitro*. In this assay, trastuzumab alone or in combination with pertuzumab has previously shown additive cardiotoxicity when administered to cells together with the anthracycline doxorubicin, toxicity that is clinically manifested in BC patients (Bria et al., 2008). Consistent with its heterodimer specificity, PB4188 displayed no additive toxicity with the anthracycline doxorubicin on adult cardiomyocytes (Figure 3E).

HER2/HER3 heterodimerization leads to cellular proliferation via phosphorylation of proteins in the MAPK and PI3K signaling pathways. We used antibody array to study the phosphorylation status of these proteins in BC cells incubated with HRG. SKBR-3 cells incubated for 24 hr under HRG stress conditions displayed enhanced activation of the PI3K signaling pathway, including a 3-fold increase in Akt phosphorylation and increased phosphorylation of S6 RP, PRAS40, and Erk1/2 (Figure 3F). PB4188 effectively blocked the changes in cellular phosphorylation events caused by HRG incubation in contrast to the combination of T + P*-treated cells. In particular, the large increase in Akt phosphorylation at Ser^{473} was similar between cells treated with T + P* and negative control, but was completely inhibited by PB4188. The differential effect of PB4188 on HRG-induced intracellular signaling at 24 hr was confirmed by western blot analysis on a second HER2-amplified cell line, N87 (Figure 3G). PB4188 fully inhibited the HRG-induced phosphorylation of HER3 and Akt, which in the case of Akt was time dependent. Similar to its anti-proliferative activity (Figure 2D), the combination T + P* could not inhibit Akt phosphorylation induced by HRG stress conditions (Figure 3G). Collectively, these data show that PB4188 selectively inhibits HRG-mediated downstream signaling events induced by the HER2/HER3 heterodimer.

The HER2 Binding Arm of PB4188 Is the Main Determinant of Binding Avidity and Facilitates Tumor Targeting

The binding of PB4188 was compared with trastuzumab and AMG888* on BC cell lines expressing different levels of HER2 using FACS analysis. PB4188 staining was higher than that of trastuzumab on all BC cell lines tested, regardless of their HER2 expression level (Figure S4A). Furthermore, the binding pattern of the bispecific PB4188 was similar to that of a monovalent bAb IgG control that combines the HER2 Fab arm of PB4188 with a Fab arm specific for tetanus toxoid (TT), an irrelevant target (Figure 4A). These data suggest that monovalent interaction with HER2, rather than avidity that might be associated with the binding of both HER2 and HER3 on the cell surface, leads to the increased staining intensity observed compared with trastuzumab. A finding that may result from a one-to-one relationship between target and binding arm, increasing the absolute number of IgG molecules that can bind to the cell surface.

In cancer cell lines, genetic aberrations such as gene amplification frequently result in levels of surface expression of HER2 much higher than those of HER3 (Schoeberl et al., 2009). In *ERBB2*-amplified cancer cells, expression of HER2 can result in as much as 1.2 million copies, whereas HER3 is expressed in numbers below 100,000 copies. In line with these observations, the binding of AMG888* to the panel of *ERBB2*-amplified BC cells in our experiments was lower than that of trastuzumab (Figure 4A). This was, however, not the case for MCF-7 cells, which are classified as HER2-low and express more balanced levels of HER2 and HER3.

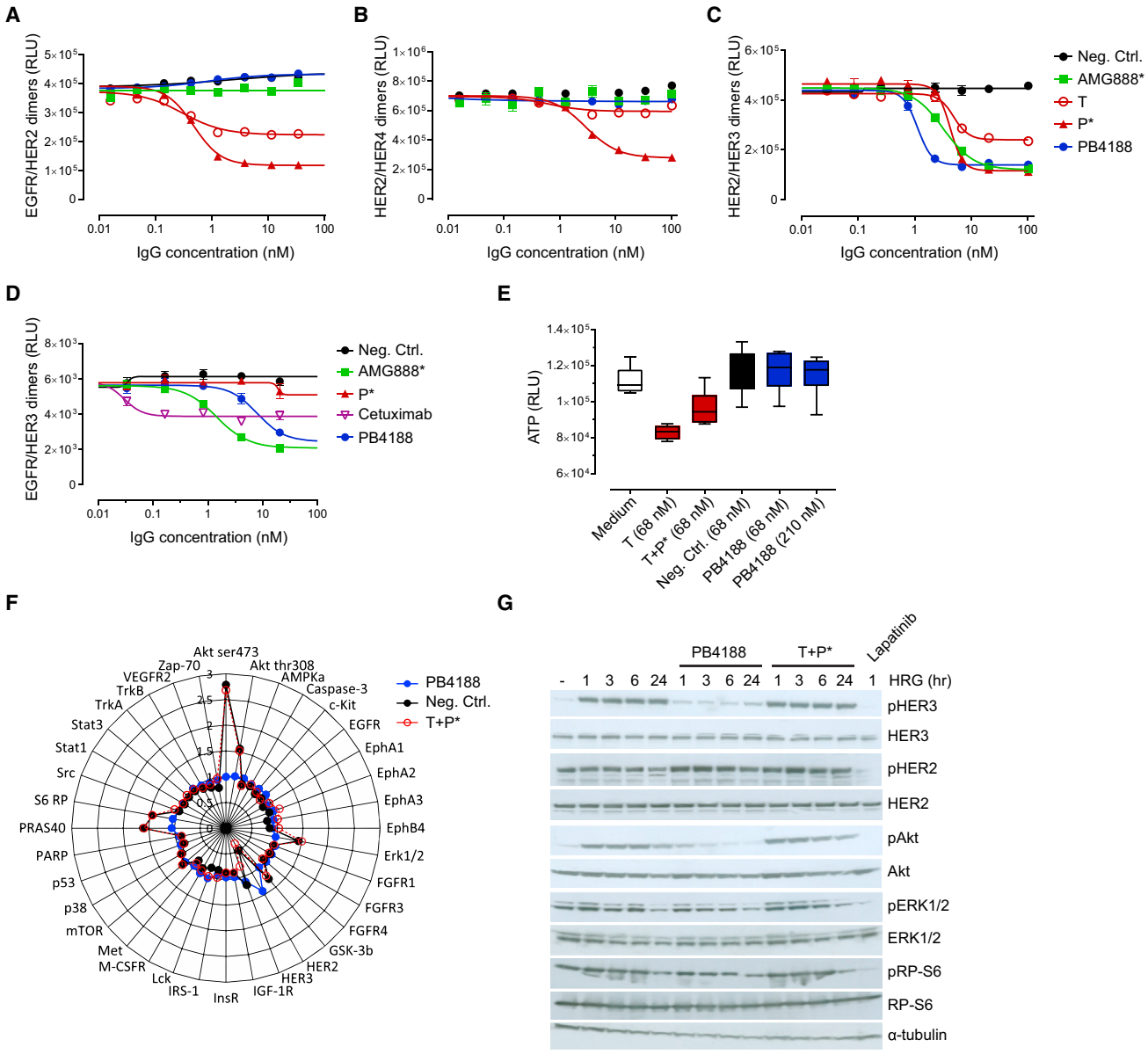

Figure 3. Selectivity of PB4188 for HER2/HER3 Signaling

(A–D) PathHunter assays to measure ligand-induced dimerization of EGFR/HER2 (A), HER2/HER4 (B), HER2/HER3 (C), and EGFR/HER3 (D). Cells were stimulated with an EC80 concentration of EGF (A) or HRG (B–D) and titrations of the indicated antibodies.

(E) Human stem cell-derived cardiomyocytes were incubated with the indicated antibodies in combination with doxorubicin. Cell viability was determined by measuring cellular ATP.

(F) SKBR-3 cells cultured in serum-free medium were supplemented with 12.5 nM HRG and the indicated antibodies. Twenty-four hours later, protein lysates were analyzed with PathScan array.

(G) Phosphorylated (p prefixed) and total levels of signaling proteins after HRG stimulation (12.5 nM) in N87 cells analyzed by western blot. T, trastuzumab; P*, pertuzumab*; T + P*, equimolar combination of trastuzumab plus pertuzumab*. Data in (A–D) are represented as means ± SEM. Boxes in (E) show the middle quartile (25%–75%); horizontal bars represent the median; whiskers show the maximum and minimum values in the dataset.

To quantify the binding of PB4188 to natively expressed HER2 and HER3, we incubated *ERBB2*-amplified cell lines with radiolabeled antibodies and determined dissociation constants (K_D). The affinity of trastuzumab measured with this approach (Table 1) was similar to that previously reported (K_D = 5 nM, product information sheet). In the BT-474 cell line, binding of the monovalent HER2xTT bAb was almost identical to that of PB4188, while the affinity of the monovalent HER3xTT bispecific was more than 10-fold higher. A similar pattern was observed in the SKBR-3 cell line. These data suggest that the overall avidity of PB4188 binding is determined by the interaction with HER2.

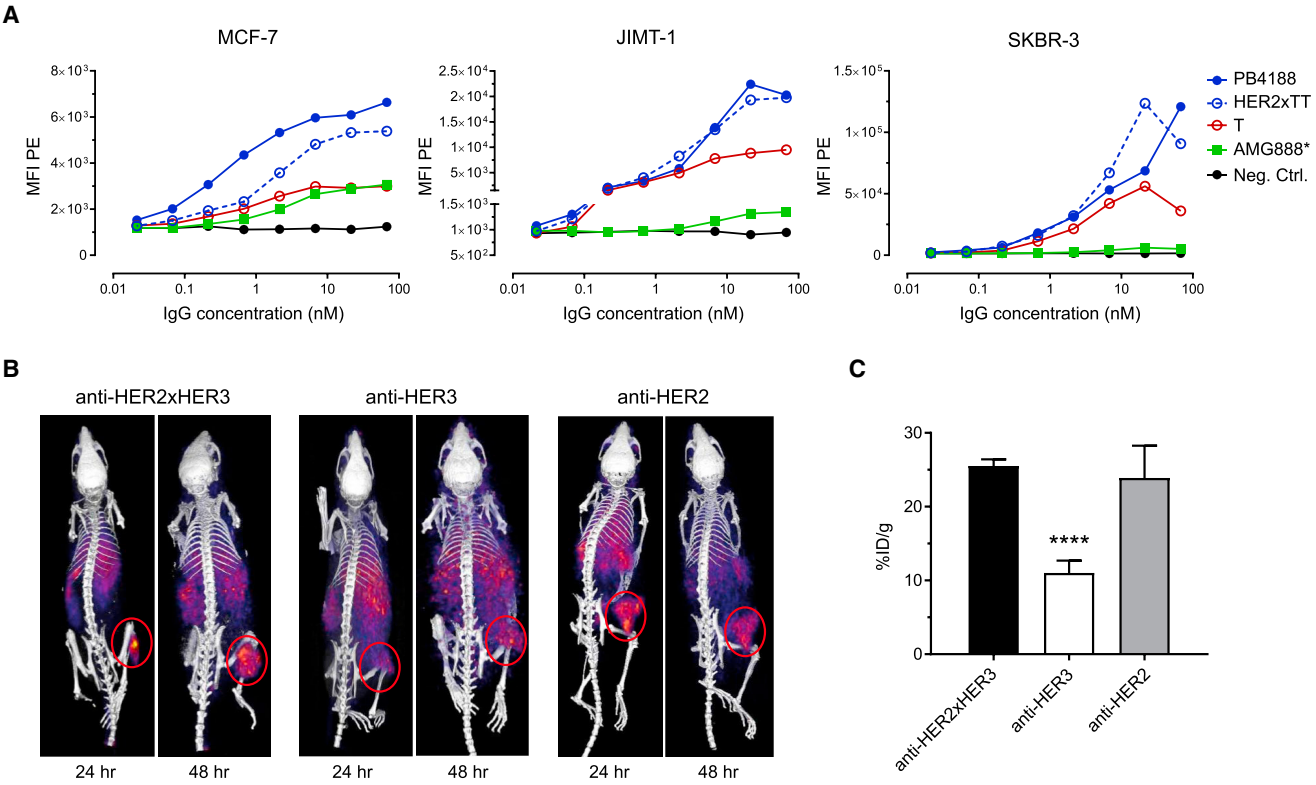

Figure 4. Increased Targeting Specificity of PB4188

(A) Titration curves of the indicated antibodies in MCF-7, JIMT-1, and SKBR-3 cells. T, trastuzumab.

(B) ^{64}Cu-labeled anti-HER2xHER3 PB4188 bAb variant, or parental anti-HER2 and anti-HER3 mAbs injected in mice xenografted with JIMT-1 tumors. Micro-PET-CT imaging at 24 and 48 hr after administration (red circle).

(C) Accumulation of radiolabeled antibodies in the tumors quantified by gamma counts. %ID/g, percentage injected dose per gram tissue. Data in (A) are representative experiments. Each experiment was done at least two independent times. Data in (C) are represented as means ± SEM (n = 4 mice). ****$p < 0.0005$ derived via unpaired t test. See also Figure S4.

Because of lower HER3 expression levels on tumors, bAbs such as PB4188 may have an advantage over HER3 mAbs when targeting HER2/HER3 heterodimers. To address this question *in vivo*, we carried out a biodistribution study to compare PB4188 and its HER2 and HER3 parental mAbs in terms of binding with xenografted tumors in mice. Micro-PET imaging using conjugated variants of bAb PB4188, and parental mAbs PG3958 and PG3178, demonstrated that tumor accumulation of antibody was higher for the PB4188 variant bAb than for the mAb that had two identical HER3 Fab binding arms (Figure 4B). Gamma-counter quantification of radioactivity confirmed that tumor levels of the PB4188 variant were 2.5-fold higher than for the parental HER3 mAb, and similar to levels of the parental HER2 mAb (Figure 4C). Overall, our *in vitro* and *in vivo* data indicated that a HER2-mediated interaction is responsible for PB4188 enhanced binding to tumor cells, resulting in more effective targeting of HER2/HER3 heterodimers.

Several lines of evidence suggest that the anti-tumor activity of trastuzumab may require recruitment of immune effector cells (Musolino et al., 2008). To exploit this mechanism and leverage the enhanced binding observed on HER2-amplified tumor cell lines *in vitro*, and the ability to target HER2 *in vivo*, a low-fucosylated variant of PB4188 (PB4188^{LF}) was generated. Reduction of IgG1 fucosylation increases the affinity to Fc receptors and thereby maximizes antibody-dependent cellular cytotoxicity (ADCC) activity (Mori et al., 2007). PB4188^{LF} was tested for ADCC activity in chromium-release assays using peripheral blood mononuclear cells, and in commercial reporter gene assays. The ADCC activity of PB4188^{LF} was greater than that of trastuzumab or unmodified PB4188 (Figures S4B and S4C). In a separate experiment, PB4188^{LF} showed low levels of internalization on HER2-amplified SKBR-3 cells, an attribute that supports the ADCC mechanism of action (MOA) (Figure S4D).

PB4188^{LF} Inhibits HRG-Driven Tumor Growth *In Vivo* in a Dose-Dependent Manner

PB4188^{LF} was evaluated in xenograft models, where tumors were dependent on HRG for growth. In the *ERBB2*-amplified JIMT-1 model, PB4188 was over 100-fold more potent than T + P* in inhibiting JIMT-1 growth *in vitro* (Figure 5A), and significantly more potent than T + P* *in vivo* (Figure 5B), activity that was dose dependent (Figure 5C). Previous studies have shown that JIMT-1 is resistant to trastuzumab and T-DM1 inhibition (Koninki et al., 2010). This has been attributed to high HRG autocrine levels that block direct inhibition of HER2 (Gijsen et al., 2010; Ritter et al., 2007) and the action of microtubulin inhibitors (Lewis

Table 1. K_D Values for Binding Affinities of Indicated Antibodies in Two *ERBB2*-Amplified BC Cell Lines

Antibody	BT-474 (nM)	SKBR-3 (nM)
Trastuzumab	3.7 ± 0.5	1.3 ± 0.1
HER2xTT[a]	3.9 ± 0.6	2.3 ± 0.7
HER3xTT[b]	0.23 ± 0.08	0.99 ± 0.4
PB4188	3.2 ± 0.5	2.0 ± 0.4

[a]bAb combining the HER2 PB4188 parental Fab with a Fab specific for the irrelevant target tetanus toxoid (TT).
[b]bAb combining the HER3 PB4188 parental Fab with TT.

Phillips et al., 2013). Pharmacodynamic analysis of tumors harvested 24 hr after final treatment using a VeraTag assay showed a significant reduction in HER2/HER3 heterodimers and HER3/p85-PI3K complexes relative to treatment with vehicle (Figure 5D). Consistent with the downstream suppression of PI3K signaling observed *in vitro*, $PB4188^{LF}$ induced almost complete suppression of Akt phosphorylation in tumor lysates prepared during the treatment period (after two doses) or at the end (after four doses) (Figure 5E). To investigate whether PB4188-mediated tumor inhibition in this model was influenced by ADCC activity, we generated a variant bAb $PB4188^{DM}$ that lacks binding to Fcγ receptors and does not exhibit ADCC activity. When we compared the HRG-dependent inhibition of JIMT-1 tumor growth *in vivo* between $PB4188^{LF}$ and $PB4188^{DM}$, both bAbs led to similar levels of tumor inhibition, confirming that $PB4188^{LF}$ inhibits tumor growth by blocking HRG-induced HER2/HER3 signaling, with no contribution from ADCC (Figure S5).

The *in vivo* therapeutic activity of $PB4188^{LF}$ was further explored in two patient-derived xenograft (PDX) models. In the orthotopic ST1360B model, tumor cells were implanted intracranially, where endogenous HRG is present in high abundance (Kodack et al., 2017). Mice received four weekly doses of $PB4188^{LF}$ or T-DM1 (shown previously to have activity in this model in contrast to trastuzumab). Tumor size was measured periodically by MRI and animals were monitored for signs of health deterioration. During the treatment period, the survival rate of mice treated systemically with $PB4188^{LF}$ was 100%, and animals survived twice as long when treated with $PB4188^{LF}$ than with vehicle (Figure 5F). In contrast, <40% of animals treated with T-DM1 were alive at treatment completion. In the OV-10-0050 PDX model, tumor cells from an OC patient with an HRG gene fusion were implanted subcutaneously (X. Tang et al., 2016; AACR, abstract). OV-10-0050 tumors that express high levels of HRG protein were treated with $PB4188^{LF}$ once weekly over 28 days and displayed complete tumor regression, in contrast with the vehicle-treated group that showed exponential tumor growth (Figure 5G). This activity was confirmed in the MDA-MB-175-VII xenograft model that contains another HRG gene fusion (Table S5). $PB4188^{LF}$ was also investigated in xenograft models lacking autocrine or paracrine HRG/HER3 activation, and no significant reduction in tumor growth was observed in such settings (Table S5). Consistent with our *in vitro* findings, we demonstrated that $PB4188^{LF}$ could suppress the growth of five HRG-dependent tumor models that are resistant or non-responsive to trastuzumab by inhibiting the HER3/PI3K signaling pathway.

The Activity of PB4188 under Ligand Stress Conditions Is Dependent on a Specific Combination of HER2 and HER3 Epitopes

Like many of the most active bAbs in the large panel from which it was selected, PB4188 has a Fab arm that binds to domain I of HER2. To determine whether PB4188 activity was dependent on its ability to bind to domain I of HER2, we combined the HER3-targeting arm (MF3178) of PB4188 with different HER2-targeting arms. We selected eight HER2 Fabs from the original panel (based on binding and functional activity), two for each of the four HER2 domains. BAbs were tested in *ERBB2*-amplified N87 cells and HER2-low MCF-7 cells stimulated with submaximal (Figure 6A) or supramaximal (Figure 6B) HRG concentrations. In all cases, bAbs containing an HER2 Fab specific for domain I were more potent in reducing cell proliferation than bAbs targeting other HER2 domains. In the cell lines incubated with submaximal HRG concentrations, bAbs targeting HER2 domain II, III, or IV showed some proliferation inhibition activity, but they were not as potent as the domain I-targeting bAbs (Figure 6A). In this set of experiments, the level of HER2 on the cell surface also had an impact on proliferation inhibition. At submaximal concentrations of HRG, MCF-7 cells were similarly inhibited by all bAbs (Figure 6A). However, in the HER2-amplified N87 cells, the HER2 domain I-targeting bAbs showed higher potency and stronger efficacy than bAbs binding to other HER2 domains. Under ligand stress conditions, these differences were even clearer: only bAbs binding domain I of HER2 were able to reduce proliferation regardless of HER2 expression level (Figure 6B).

The Potent Blocking Activity of HRG/HER3 Signaling by PB4188 Is due to Its Mode of Binding

Our *in vitro* functional data suggested that PB4188's anti-tumor activity relates to its interaction with a specific combination of HER2 and HER3 domains. To gain further molecular insight, we determined the crystallographic structures of HER2 Fab MF3958 in complex with the HER2 ECD (residues T23-T652, UniProt) (3.0 Å) and HER3 Fab MF3178 in complex with HER3 ECD (residues S20-T643) (4.5 and 3.4 Å). Table S6 shows the data collection and refinement statistics. In the HER2-ECD:MF3958 complex (Figure 7A), the domain organization of HER2 is very similar to previously described structures (PDB: 3BE1, 1N8Y, 1N8Z, 3MZW, 3N85, and 1S78), with a root-mean-square deviation (RMSD) for the Cα-backbone atoms ranging from 0.4 to 0.8 Å. MF3958 binds to HER2 at the C-terminal part of domain I through a shallow interaction surface that buries 683 $Å^2$, mediated almost entirely by the three complementarity-determining regions (CDRs) of the Fab VH (Table S7; Figures S6A and S6B). The epitope is composed of two peptide stretches within HER2, residues 143–147 and 160–181 (Figure 7B). These observations are in line with the findings of the alanine scanning experiment that identified the functional importance of HER2 residues T144, R166, R181, P172, and G179 (Figure S6C). The region recognized by MF3958 differs from that of pertuzumab and trastuzumab Fabs, which bind residues located in domains II (pertuzumab) and IV (trastuzumab) of HER2 (Figures S6D and S6E). The MF3958 epitope partially overlaps with that of a previously described HER2-targeting scFv construct A21 (Zhou et al., 2011), which binds three patches at the

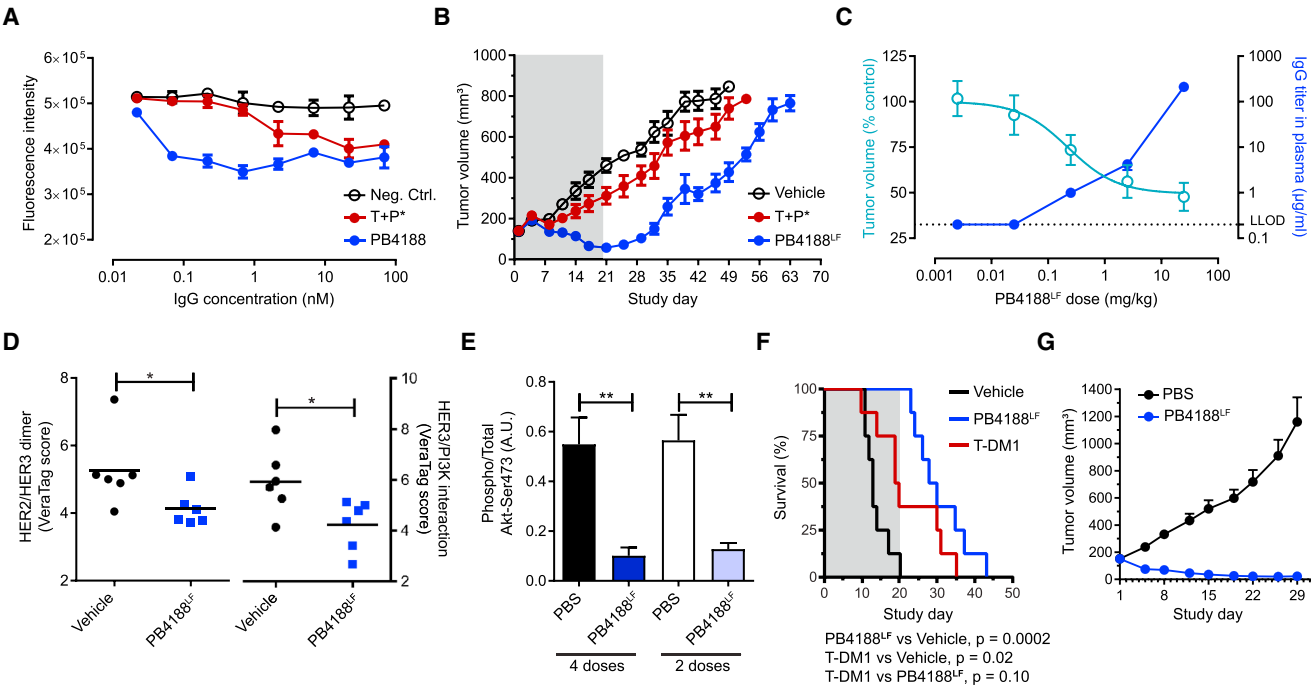

Figure 5. Superior *In Vivo* Anti-tumor Activity of PB4188^{LF}

(A) JIMT-1 cells cultured in soft agar were incubated with the indicated antibodies for 8 days before measuring proliferation.

(B) Tumor volume of JIMT-1 xenografts treated weekly (gray shading) with the indicated antibodies.

(C) Correlation between tumor volume (normalized against the vehicle group) and antibody levels in the serum of JIMT-1 xenografts treated with increasing doses of PB4188^{LF}. LLOD, lower limit of detection.

(D) HER2/HER3 dimers and HER3/PI3K complexes were quantified with VeraTag assay in JIMT-1 xenografts treated with PB4188^{LF} or vehicle. Horizontal bars represent the mean VeraTag score.

(E) Levels of phosphorylated Akt were quantified by Luminex in JIMT-1 tumors harvested from mice treated with two or four doses of PBS or PB4188^{LF}.

(F) NRMI nude mice injected intracranially with ST1360B PDX cells were treated weekly (gray shading) with PB4188^{LF}, T-DM1, or vehicle (n = 8 mice). Survival data analyzed with log rank test adjusted for multiple comparisons (Bonferroni), where $p < 0.017$ is considered significant.

(G) Tumor volume of OV-10-0050 PDX treated weekly for 28 days with PB4188^{LF} or PBS. T + P*, equimolar combination of trastuzumab plus pertuzumab*. Data in (A and B) (n = 10 mice), (C) (n = 5 mice), (E and G) (n = 8 mice) are represented as means ± SEM. *$p < 0.05$, **$p < 0.01$ derived via unpaired t test.

See also Figure S5 and Table S5.

C terminus of domain I, namely residues 100–105, 135–144, and 163–187 (Figure S6F).

In the HER3-ECD:MF3178 complex, HER3 is in its "tethered" inactive state (Figure 7C). All four ECDs (I–IV) of HER3 are observed in the electron density of the 4.5-Å resolution structure, while in the 3.4-Å resolution structure almost the whole domain I of HER3 (residues M1-P260, K279-C301) has a poorly defined electron density (Figure S7A). Structural analysis was based on the structure determined at 3.4 Å resolution. The overall conformation of HER3 is similar to previously solved structures (PDB: 1M6B, 3P11, 4LEO, 4P59, and 5CUS), with an RMSD ranging from 1.0 up to 2.1 Å for the Cα-backbone atoms, reflecting minor domain reorientations. The epitope is localized on domain III of HER3. The protruding loop containing residues Y424, N425, and R426 slots into a pocket formed by light chains CDR 1 and 3 (LCDR1 and LCDR3) and HCDR3 of the Fab (Figure 7D; Table S7). The MF3178 interface buries only 426 Å^2 on the HER3 side, with the VH and the variable light chain (VL) contributing almost equally (238 Å^2 for VH and 188 Å^2 for the VL) (Figures S7B and S7C). These results confirm the importance of residue R426 that was also identified by alanine scanning (Figure S7D). Although the HER2 and HER3 Fabs of PB4188 share a single light chain (LC) in germline configuration, the LC appears to contribute significantly to the recognition of the HER3 epitope, while it is scarcely involved in binding HER2. A finding of note was that Y32 in LCDR1 contributed to the binding of both HER2 and HER3 (Table S7). Our analysis revealed that MF3178 epitope is different from all other published HER3:Fab structures (Figures S7E–S7H). For example, the epitope of the DL11 Fab (Schaefer et al., 2011), also localized in domain III, has a different conformational arrangement and involves different residues (Figure S7E). Comparison of our data with the published structure of the HER4:HRG complex (Liu et al., 2012) suggests that binding of the MF3178 Fab would be incompatible with the untethered (active) conformation of HER3 because it would cause a steric clash between domain I and MF3178. More importantly, we found that the MF3178 binding site on HER3 partially overlaps with the putative HRG binding site. These observations therefore suggest a MOA in which MF3178 binds to the inactive monomeric conformation of HER3 and blocks any interaction with HRG.

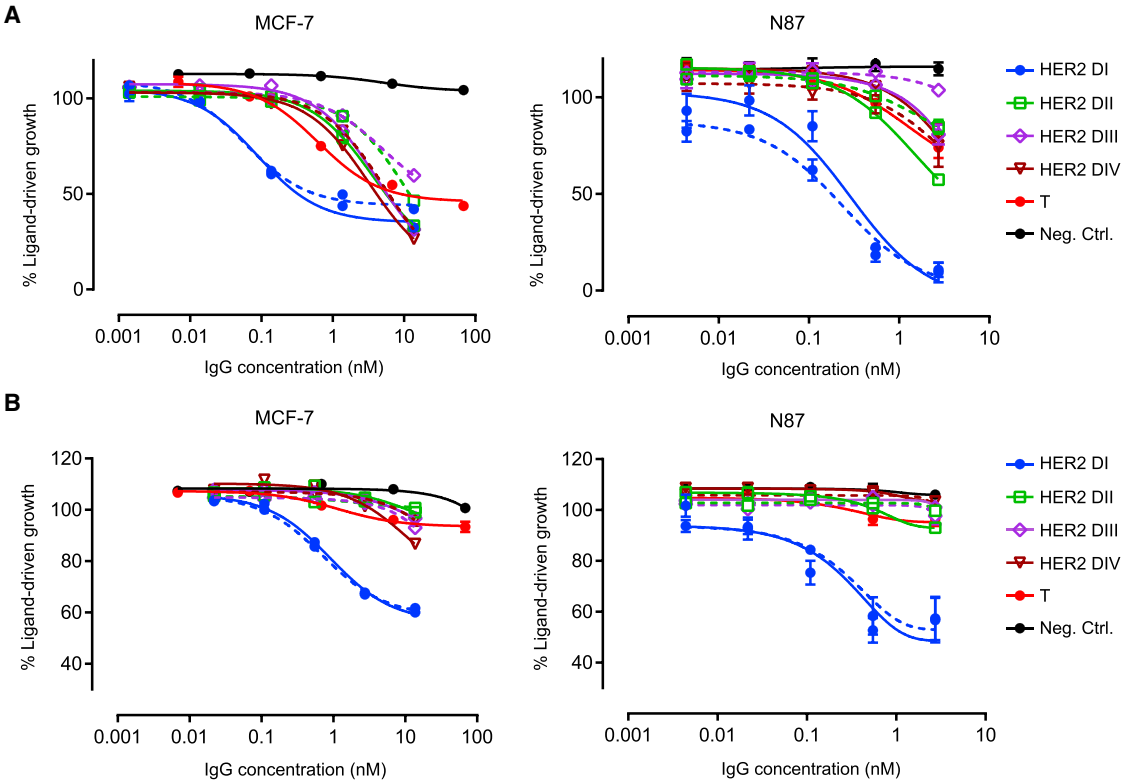

Figure 6. PB4188 Activity Is Determined by the Targeted HER2 Domain

(A and B) MCF-7 and N87 cells were stimulated with 0.125 nM (A) or 12.5 nM (B) HRG. A titration of bAbs consisting of the anti-HER3 Fab MF3178 combined with domain-specific anti-HER2 Fabs as indicated (two different HER2 Fabs per group, solid and dashed lines), and the domain IV-binding trastuzumab, was added. T, trastuzumab. Data are represented as means ± SEM.

We also carried out small-angle X-ray scattering (SAXS) on the HER2-ECD:HER3-ECD:PB4188 complex, to analyze PB4188 binding when both receptor ECDs are present in solution. By fitting the crystal structures of the HER2-ECD:MF3958 and HER3-ECD:MF3178 complexes and a representative Fc region with the SAXS *ab initio* model (Figure 7E), we could confirm that PB4188 IgG is able to bind to both HER2 and HER3 ECDs in solution at the same time, with a paratope-to-paratope span of approximately 140 Å.

DISCUSSION

We have applied a bispecific full-length IgG1 format to generate a therapeutic targeting HER2 and HER3 in tumors with *de novo* or acquired HRG/HER3 pathway upregulation. Because little is known about the optimal mechanism to achieve pharmacologically relevant inhibition with bAbs, we pursued an unbiased phenotypic screening approach with a downstream functional readout (cell growth inhibition). This allowed us to operate without making assumptions concerning affinity or epitope specificity of the bispecific IgG binding arms, or about the specific mechanistic outcome of target engagement. Using this unbiased approach, we identified several potent inhibitors of ligand-dependent proliferation that shared a number of common attributes. First, these inhibitors were capable of potent tumor cell proliferation inhibition in the presence of supramaximal concentrations of HRG—a result of sustained ligand signaling blockade. The potency and MOA demonstrated *in vitro* was verified with the selected lead candidate PB4188 in four independent and pathophysiologically relevant xenograft models, and appeared to be dose dependent and correlated with relevant pharmacodynamic factors such as Akt phosphorylation. Second, the collection of bAbs capable of supramaximal HRG inhibition all contained a HER2 Fab that bound to domain I. The therapeutic HER2-targeting antibodies trastuzumab and pertuzumab do not bind to HER2 in domain I, but in domains IV (trastuzumab) and II (pertuzumab). Given the potent inhibition of HER2 signaling by trastuzumab, bAbs containing domain IV-binding Fabs combined with HER3-inhibiting Fabs might have been expected to have synergistic inhibitory activity. Indeed one of the most potent bAbs identified in the initial *in vitro* and *in vivo* screens was an antibody that contained a domain IV-binding HER2 Fab. However, this bAb failed to inhibit proliferation at supramaximal ligand concentrations, unlike the lead bispecific PB4188.

To gain mechanistic insight into the potent inhibition of HRG/HER3 signaling by PB4188, we resolved the crystal structures of both parental Fabs in complex with their target proteins. The HER3 Fab of PB4188 binds HER3 in its tethered conformation, and its epitope partially overlaps with the putative HRG binding pocket. It is therefore likely that PB4188 blocks HRG binding to HER3 due to steric hindrance, which is consistent with the

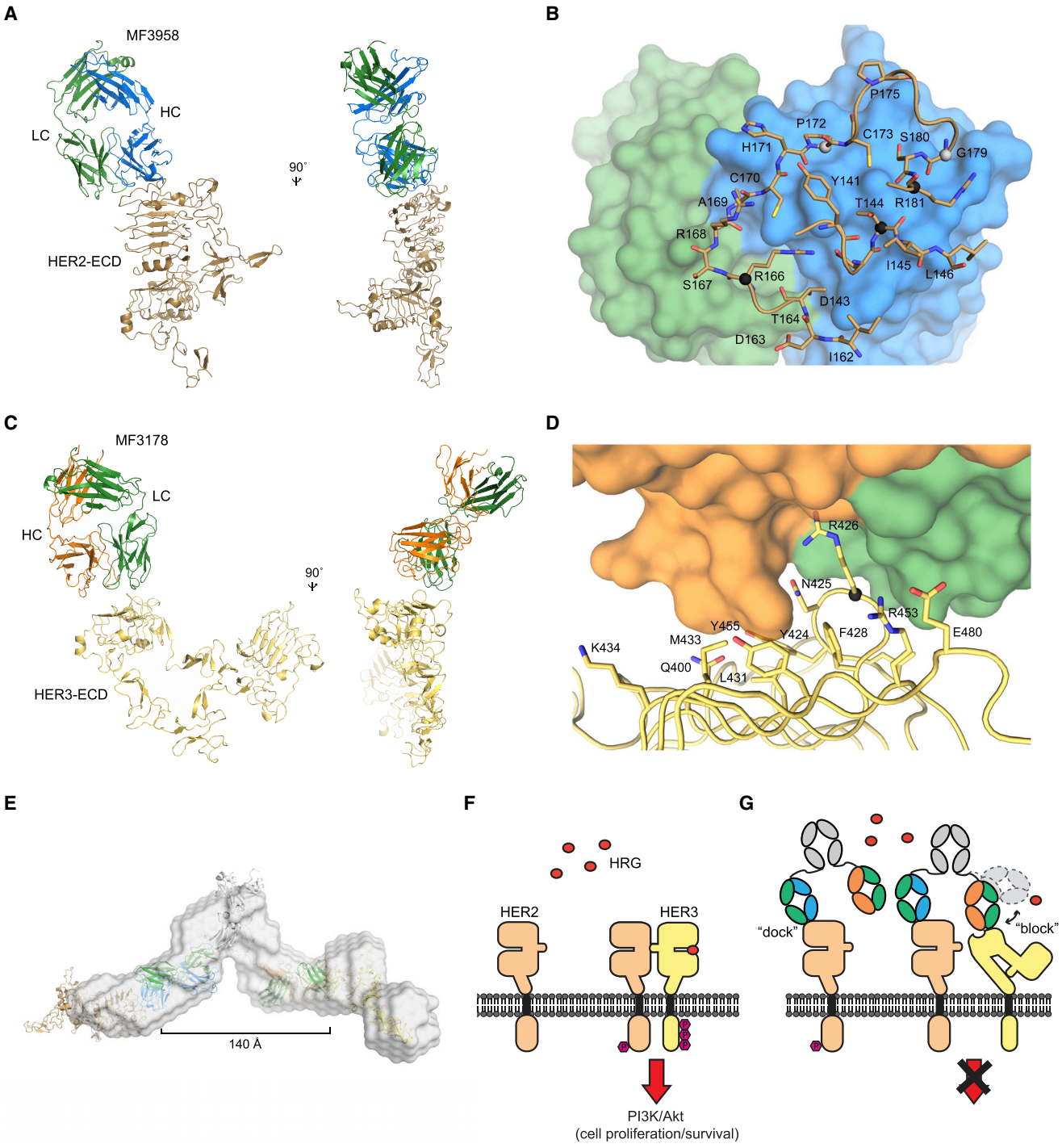

Figure 7. Structural Investigation of PB4188 Mode of Binding

(A) Structure of HER2-ECD:MF3958 complex in two orthogonal views. HER2 is beige, the MF3958 HC is blue, and the LC is green.

(B) Bottom view of the HER2-ECD:MF3958 interaction. HER2 residues shown as sticks; MF3958 shown as surface, color scheme as in (A). Spheres indicate residues identified by alanine scanning as critical (black) and "secondary" critical (gray).

(C) Structure of HER3-ECD:MF3178 complex in two orthogonal views. HER3 is yellow, the MF3178 HC is orange, and the LC is green.

(D) Side view of HER3-ECD:MF3178 interaction. HER3 residues shown as sticks; MF3178 shown as surface, color scheme as in (C). A black sphere indicates the residue identified by alanine scanning as critical.

(E) Superposition of a representative SAXS *ab initio* model of the HER2-ECD:HER3-ECD:PB4188 complex (shown as gray surface) on the crystal structures of HER2-ECD:MF3958, HER3-ECD:MF3178, color scheme as in (A and C), and an Fc region (gray, PDB: 1HZH). The black line indicates the paratope-to-paratope reach.

(F and G) Graphical representation of HRG-mediated signaling in absence (F) and in presence (G) of PB4188. See also Figures S6, S7, Tables S6, and S7.

ability of parental HER3 mAb PG3178 to inhibit ligand-driven proliferation at submaximal concentrations of HRG. The epitope of the PB4188 HER2 Fab is on top of HER2 domain I, i.e., at a location the most distal from the cell surface. The HER2 mAb A21 also binds to this region of domain I, and has been shown effective in binding and crosslinking adjacent HER2 molecules (Zhou et al., 2011). Thus, binding of PB4188 to HER2 domain I likely leaves the Fab HER3 arm free to orient itself for interactions with adjacent HER3, blocking ligand-driven heterodimer formation.

Based on our experimental data and structural analysis, we propose that PB4188 uses a "dock & block" mechanism to inhibit HRG-driven proliferation of HER2-amplified tumors, even at supramaximal concentrations of HRG (Figures 7F and 7G). HER2 amplification (Junttila et al., 2009) or ligand availability (Landgraf and Eisenberg, 2000) favors the recruitment of HER3 out of catalytically inactive oligomeric complexes, shifting the equilibrium toward signaling-competent heterodimers. Heterodimerization of HER3 with HER2 also increases the affinity of HER3's binding pocket for HRG, favoring the stability of the dimer (Sliwkowski et al., 1994). In our model, the HER2 Fab of PB4188 "docks" and saturates the available HER2 binding sites on tumor cells, effectively increasing the local concentration of the HER3 Fab. Since the binding of PB4188 to HER2 is independent of the presence of HRG, PB4188 maintains its advantageous localization effects at high HRG concentrations to "block" HRG binding to HER3, thus preventing formation of signaling dimers and clusters thereof. In contrast, as shown in this study, anti-HER2 and anti-HER3 mAbs, or equimolar combinations of these monospecific antibodies, are unable to inhibit HER3 signaling when HRG exceeds a threshold concentration (5–10 nM). The previously described HER2xHER3 bispecific scFv construct MM-111 (McDonagh et al., 2012) binds with high avidity to HER2-positive cells and can effectively block submaximal ligand-driven proliferation, but not supramaximal activation. MM-111 was designed, based on modeling, to have a higher-affinity HER2 arm compared with its HER3 arm (K_D = 16 nM) to target HER2-amplified tumors. We have demonstrated that tumor targeting of PB4188, *in vitro* and *in vivo*, is unaffected by the high-affinity binding of its HER3 arm (K_D = 0.2 nM), but that this attribute and the avidity advantage conferred by HER2 targeting are required to overcome the high-affinity interaction between HRG and the HER2/HER3 dimer.

A number of therapeutic agents targeting the HRG/HER3 pathway are under clinical evaluation but to date have not generated clinical proof of concept (Paz-Arez et al., 2017; Reynolds et al., 2014; Sequist et al., 2014). One explanation for this outcome is that the HER3 mAbs currently evaluated do not have the potency to fully inhibit the HRG/HER3 pathway. In an OC model, it was shown that short hairpin RNA knockdown could induce tumor regression, but inhibition by the HER3 mAb MM-121 was not sufficiently potent to reduce tumor volume (Sheng et al., 2010). This is consistent with other studies demonstrating that complete blockade of HER3 signaling is required to arrest growth of HER2/HER3-dependent tumor lines (Garrett et al., 2013; Sergina et al., 2007), and with our data where none of the HER3 mAb analogs, including MM-121, were capable of inhibiting proliferation under "ligand stress conditions." Another potential factor is a lack of appropriate selection criteria for patient populations in these trials. A number of studies have demonstrated that increased baseline levels of biomarkers affecting the HRG/HER3 pathway, such as HRG or HER3 expression in tumors or circulating HRG, are prognostic for poorer outcome and/or suggestive of better treatment response (Liu et al., 2016; Nonagase et al., 2016; Pradeep et al., 2014; Yonesaka et al., 2017). However, not all studies have reported a significant correlation (Mukai et al., 2016), and none of these methods measured HRG/HER3 pathway activation directly, which may contribute to discrepancies between studies. Recently developed approaches, such as proximity assays to measure association of HER3 and PI3K (Mukherjee et al., 2011) or downstream phosphorylation (Sheng et al., 2010), could be applied to improve patient stratification and enrichment of responders.

The development candidate of PB4188, MCLA-128, is currently undergoing clinical evaluation in patient populations where evidence of HRG/HER3 pathway activation has been reported, including HER2-amplified and ER-positive BC, gastric cancer, OC, endometrial cancer, and NSCLC. As a single agent, MCLA-128 is well tolerated with no severe gastrointestinal toxicities or evidence of clinically significant cardiovascular events, and durable responses have been observed in heavily pretreated patients (M. Alsina et al., 2017; ASCO, abstract; E. Calvo et al., 2016; AACR, abstract). Evaluation of an extensive biomarker panel is ongoing in these patients to associate evidence of HRG/HER3 pathway activation with responses.

In conclusion, based on its unique mode of action and differentiated preclinical potency, we expect that MCLA-128 will provide significant benefit to patients in settings where the current standard of care is not effective due to HRG/HER3 pathway activation. The "*cis*" mode of action that we describe here may be broadly applicable to the bAb class of therapeutics, unlocking biological activity that cannot be achieved using mAbs. Our experience suggests that the discovery of bAbs with these modes of action is highly dependent on unbiased screening and on the selection of appropriate functional readouts.

STAR★METHODS

Detailed methods are provided in the online version of this paper and include the following:

- KEY RESOURCES TABLE
- CONTACT FOR REAGENT AND RESOURCE SHARING
- EXPERIMENTAL MODEL AND SUBJECT DETAILS
  - Mouse Models
  - Cell Lines
- METHOD DETAILS
  - Recombinant Proteins and Constructs
  - Immunizations, Phage Library Generation and Selection
  - Humanization
  - Cell Line Proliferation Assays
  - Proliferation Inhibition Assays
  - Cell Cycle Analysis in HRG-stimulated Cell Lines
  - PathHunter Dimerization Assay
  - In Vitro Cardiomyocyte Viability Assay
  - Phosphorylation Assays

- Cell Surface Binding Measured by FACS
- Affinity Determination
- Antibody-dependent Cytotoxicity Assays
- Internalization Assay
- Xenograft Studies
- HER Expression and Downstream Phosphorylation
- Epitope Mapping
- X-ray Crystallography
- SAXS

- QUANTIFICATION AND STATISTICAL ANALYSIS
- DATA AND SOFTWARE AVAILABILITY

SUPPLEMENTAL INFORMATION

Supplemental Information includes eight figures and eight tables can be found with this article online at https://doi.org/10.1016/j.ccell.2018.04.003.

ACKNOWLEDGMENTS

We would like to thank Leo Price and Maarten Klop at Ocello for their contributions to the 3D *in vitro* models; Stefan Braam at Pluriomics for his contribution to the cardiomyocyte *in vitro* experiments; Carsten H. Nielsen and Mette M. Jensen at Minerva Imaging for their contributions to the design and execution of the intracranial ST1360B PDX study; Matt Harris and Amos Hedt at Clarity Pharmaceuticals for their contributions to the *in vivo* imaging study; U-Protein Express BV for the provision of protein expression facilities; Ron Schackmann for database mining and critical reading of the manuscript; Andres Sirulnik, Ernesto Wasserman, Afrodite Lourbakos, Livio Trusolino, and Eduard Batlle for critical reading of the manuscript; Sally Hill for writing and editing assistance; the European Synchrotron Radiation Facility (ESRF) and the Swiss Light Source (SLS) for the provision of synchrotron radiation facilities; and beamline scientists of the ESRF, SLS, and the European Molecular Biology Laboratory for assistance. Financial support was provided by the ManiFold project (grant no. 317371) and the BioStruct-X project (grant no. 283570) embedded in the European Union's Seventh Framework Programme (FP7/2007-2013), and by the Eurostars ReBAT project (grant no. E!6121).

AUTHOR CONTRIBUTIONS

T.V., R.N., and L.J.A.H. contributed to the antibody isolation and characterization experiments. D.M., E.R., and T.G. performed the *in vitro* experiments. C.A.W.G., D.M., E.R., T.G., J.d.K., and M.T. contributed to the *in vitro* and *in vivo* experiments. C.D.N. performed the structural investigation. C.A.W.G., C.D.N., D.M., E.R., T.G., L.J.A.H., J.d.K., P.G., and M.T. conducted data analysis. C.A.W.G., D.M., T.L., J.d.K., P.G., and M.T. conceived the study. M.T., C.A.W.G., D.M., C.D.N., and P.G. wrote the paper.

DECLARATION OF INTERESTS

At the time this work was completed, C.A.W.G., D.M., E.R., T.G., L.J.A.H., T.V., R.N., T.L., J.d.K., and M.T. were employees and shareholders of Merus NV.

Received: July 31, 2017
Revised: February 26, 2018
Accepted: April 9, 2018
Published: May 14, 2018

REFERENCES

Adams, P.D., Afonine, P.V., Bunkóczi, G., Chen, V.B., Davis, I.W., Echols, N., Headd, J.J., Hung, L.W., Kapral, G.J., Grosse-Kunstleve, R.W., et al. (2010). PHENIX: a comprehensive Python-based system for macromolecular structure solution. Acta Crystallogr. D Biol. Crystallogr. *66*, 213–221.

Battye, T.G., Kontogiannis, L., Johnson, O., Powell, H.R., and Leslie, A.G. (2011). iMOSFLM: a new graphical interface for diffraction-image processing with MOSFLM. Acta Crystallogr. D Biol. Crystallogr. *67*, 271–281.

Berlin, J., Keedy, V.L., Janne, P.A., Yee, L., Rizvi, N.A., Jin, X., Copigneaux, C., Hettmann, T., Beaupre, D.M., and LoRusso, P. (2011). A first-in-human phase I study of U3-1287 (AMG 888), a HER3 inhibitor, in patients (pts) with advanced solid tumors. J. Clin. Oncol. *29*, 3026.

Bria, E., Cuppone, F., Milella, M., Verma, S., Carlini, P., Nistico, C., Vaccaro, V., Rossi, A., Tonini, G., Cognetti, F., and Terzoli, E. (2008). Trastuzumab cardiotoxicity: biological hypotheses and clinical open issues. Expert Opin. Biol. Ther. *8*, 1963–1971.

Capparelli, C., Rosenbaum, S., Berger, A.C., and Aplin, A.E. (2015). Fibroblast-derived neuregulin 1 promotes compensatory ErbB3 receptor signaling in mutant BRAF melanoma. J. Biol. Chem. *290*, 24267–24277.

Chakrabarty, A., Sanchez, V., Kuba, M.G., Rinehart, C., and Arteaga, C.L. (2012). Feedback upregulation of HER3 (ErbB3) expression and activity attenuates antitumor effect of PI3K inhibitors. Proc. Natl. Acad. Sci. USA *109*, 2718–2723.

Chandarlapaty, S., Sawai, A., Scaltriti, M., Rodrik-Outmezguine, V., Grbovic-Huezo, O., Serra, V., Majumder, P.K., Baselga, J., and Rosen, N. (2011). AKT inhibition relieves feedback suppression of receptor tyrosine kinase expression and activity. Cancer Cell *19*, 58–71.

de Kruif, J., Boel, E., and Logtenberg, T. (1995). Selection and application of human single chain Fv antibody fragments from a semi-synthetic phage antibody display library with designed CDR3 regions. J. Mol. Biol. *248*, 97–105.

de Kruif, J., Kramer, A., Visser, T., Clements, C., Nijhuis, R., Cox, F., van der Zande, V., Smit, R., Pinto, D., Throsby, M., and Logtenberg, T. (2009). Human immunoglobulin repertoires against tetanus toxoid contain a large and diverse fraction of high-affinity promiscuous V(H) genes. J. Mol. Biol. *387*, 548–558.

De Nardis, C., Hendriks, L.J.A., Poirier, E., Arvinte, T., Gros, P., Bakker, A.B.H., and de Kruif, J. (2017). A new approach for generating bispecific antibodies based on a common light chain format and the stable architecture of human immunoglobulin G1. J. Biol. Chem. *292*, 14706–14717.

Emsley, P., Lohkamp, B., Scott, W.G., and Cowtan, K. (2010). Features and development of Coot. Acta Crystallogr. D Biol. Crystallogr. *66*, 486–501.

Evans, P.R., and Murshudov, G.N. (2013). How good are my data and what is the resolution? Acta Crystallogr. D Biol. Crystallogr. *69*, 1204–1214.

Fernandez-Cuesta, L., Plenker, D., Osada, H., Sun, R., Menon, R., Leenders, F., Ortiz-Cuaran, S., Peifer, M., Bos, M., Dassler, J., et al. (2014). CD74-NRG1 fusions in lung adenocarcinoma. Cancer Discov. *4*, 415–422.

Franke, D., and Svergun, D.I. (2009). DAMMIF, a program for rapid ab-initio shape determination in small-angle scattering. J. Appl. Crystallogr. *42*, 342–346.

Garner, A.P., Bialucha, C.U., Sprague, E.R., Garrett, J.T., Sheng, Q., Li, S., Sineshchekova, O., Saxena, P., Sutton, C.R., Chen, D., et al. (2013). An antibody that locks HER3 in the inactive conformation inhibits tumor growth driven by HER2 or neuregulin. Cancer Res. *73*, 6024–6035.

Garrett, J.T., Sutton, C.R., Kuba, M.G., Cook, R.S., and Arteaga, C.L. (2013). Dual blockade of HER2 in HER2-overexpressing tumor cells does not completely eliminate HER3 function. Clin. Cancer Res. *19*, 610–619.

Gassmann, M., Casagranda, F., Orioli, D., Simon, H., Lai, C., Klein, R., and Lemke, G. (1995). Aberrant neural and cardiac development in mice lacking the ErbB4 neuregulin receptor. Nature *378*, 390–394.

Gijsen, M., King, P., Perera, T., Parker, P.J., Harris, A.L., Larijani, B., and Kong, A. (2010). HER2 phosphorylation is maintained by a PKB negative feedback loop in response to anti-HER2 herceptin in breast cancer. PLoS Biol. *8*, e1000563.

Hegde, G.V., de la Cruz, C.C., Chiu, C., Alag, N., Schaefer, G., Crocker, L., Ross, S., Goldenberg, D., Merchant, M., Tien, J., et al. (2013). Blocking NRG1 and other ligand-mediated Her4 signaling enhances the magnitude and duration of the chemotherapeutic response of non-small cell lung cancer. Sci. Transl. Med. *5*, 171ra118.

Holbro, T., Beerli, R.R., Maurer, F., Koziczak, M., Barbas, C.F., 3rd, and Hynes, N.E. (2003). The ErbB2/ErbB3 heterodimer functions as an oncogenic unit: ErbB2 requires ErbB3 to drive breast tumor cell proliferation. Proc. Natl. Acad. Sci. USA *100*, 8933–8938.

Junttila, T.T., Akita, R.W., Parsons, K., Fields, C., Lewis Phillips, G.D., Friedman, L.S., Sampath, D., and Sliwkowski, M.X. (2009). Ligand-independent HER2/HER3/PI3K complex is disrupted by trastuzumab and is effectively inhibited by the PI3K inhibitor GDC-0941. Cancer Cell *15*, 429–440.

Kodack, D.P., Askoxylakis, V., Ferraro, G.B., Sheng, Q., Badeaux, M., Goel, S., Qi, X., Shankaraiah, R., Cao, Z.A., Ramjiawan, R.R., et al. (2017). The brain microenvironment mediates resistance in luminal breast cancer to PI3K inhibition through HER3 activation. Sci. Transl. Med. *9*, eaal4682.

Konarev, P.V., Kikhney, A.G., Sokolova, A.V., Svergun, D.I., and Volkov, V.V. (2003). Manipulations with experimental 1D small-angle scattering data. J. Appl. Crystallogr. *36*, 1277–1282.

Koninki, K., Barok, M., Tanner, M., Staff, S., Pitkanen, J., Hemmila, P., Ilvesaro, J., and Isola, J. (2010). Multiple molecular mechanisms underlying trastuzumab and lapatinib resistance in JIMT-1 breast cancer cells. Cancer Lett. *294*, 211–219.

Kontermann, R.E., and Brinkmann, U. (2015). Bispecific antibodies. Drug Discov. Today *20*, 838–847.

Landgraf, R., and Eisenberg, D. (2000). Heregulin reverses the oligomerization of HER3. Biochemistry *39*, 8503–8511.

Lee-Hoeflich, S.T., Crocker, L., Yao, E., Pham, T., Munroe, X., Hoeflich, K.P., Sliwkowski, M.X., and Stern, H.M. (2008). A central role for HER3 in HER2-amplified breast cancer: implications for targeted therapy. Cancer Res. *68*, 5878–5887.

Lee, S., Greenlee, E.B., Amick, J.R., Ligon, G.F., Lillquist, J.S., Natoli, E.J., Jr., Hadari, Y., Alvarado, D., and Schlessinger, J. (2015). Inhibition of ErbB3 by a monoclonal antibody that locks the extracellular domain in an inactive configuration. Proc. Natl. Acad. Sci. USA *112*, 13225–13230.

Lewis Phillips, G.D., Fields, C.T., Li, G., Dowbenko, D., Schaefer, G., Miller, K.D., Andre, F., Burris, H.A., 3rd, Albain, K.S., Harbeck, N., et al. (2013). Dual targeting of HER2-positive cancer with trastuzumab-emtansine (T-DM1) and pertuzumab: critical role for neuregulin blockade in anti-tumor response to combination therapy. Clin. Cancer Res. *15*, 456–468.

Liu, J.F., Ray-Coquard, I., Selle, F., Poveda, A.M., Cibula, D., Hirte, H., Hilpert, F., Raspagliesi, F., Gladieff, L., Harter, P., et al. (2016). Randomized phase II trial of seribantumab in combination with paclitaxel in patients with advanced platinum-resistant or -refractory ovarian cancer. J. Clin. Oncol. *34*, 4345–4353.

Liu, P., Cleveland, T.E., Bouyain, S., Byrne, P.O., Longo, P.A., and Leahy, D.J. (2012). A single ligand is sufficient to activate EGFR dimers. Proc. Natl. Acad. Sci. USA *109*, 10861–10866.

McCoy, A.J., Grosse-Kunstleve, R.W., Adams, P.D., Winn, M.D., Storoni, L.C., and Read, R.J. (2007). Phaser crystallographic software. J. Appl. Crystallogr. *40*, 658–674.

McDonagh, C.F., Huhalov, A., Harms, B.D., Adams, S., Paragas, V., Oyama, S., Zhang, B., Luus, L., Overland, R., Nguyen, S., et al. (2012). Antitumor activity of a novel bispecific antibody that targets the ErbB2/ErbB3 oncogenic unit and inhibits heregulin-induced activation of ErbB3. Mol. Cancer Ther. *11*, 582–593.

Mirschberger, C., Schiller, C.B., Schräml, M., Dimoudis, N., Friess, T., Gerdes, C.A., Reiff, U., Lifke, V., Hoelzlwimmer, G., Kolm, I., et al. (2013). RG7116, a therapeutic antibody that binds the inactive HER3 receptor and is optimized for immune effector activation. Cancer Res. *73*, 5183–5194.

Mori, K., Iida, S., Yamane-Ohnuki, N., Kanda, Y., Kuni-Kamochi, R., Nakano, R., Imai-Nishiya, H., Okazaki, A., Shinkawa, T., Natsume, A., et al. (2007). Non-fucosylated therapeutic antibodies: the next generation of therapeutic antibodies. Cytotechnology *55*, 109–114.

Morrison, M.M., Hutchinson, K., Williams, M.M., Stanford, J.C., Balko, J.M., Young, C., Kuba, M.G., Sanchez, V., Williams, A.J., Hicks, D.J., et al. (2013). ErbB3 downregulation enhances luminal breast tumor response to antiestrogens. J. Clin. Invest. *123*, 4329–4343.

Mukai, H., Saeki, T., Aogi, K., Naito, Y., Matsubara, N., Shigekawa, T., Ueda, S., Takashima, S., Hara, F., Yamashita, T., et al. (2016). Patritumab plus trastuzumab and paclitaxel in human epidermal growth factor receptor 2-overexpressing metastatic breast cancer. Cancer Sci. *107*, 1465–1470.

Mukherjee, A., Badal, Y., Nguyen, X.T., Miller, J., Chenna, A., Tahir, H., Newton, A., Parry, G., and Williams, S. (2011). Profiling the HER3/PI3K pathway in breast tumors using proximity-directed assays identifies correlations between protein complexes and phosphoproteins. PLoS One *6*, e16443.

Muller-Tidow, C., Diederichs, S., Bulk, E., Pohle, T., Steffen, B., Schwable, J., Plewka, S., Thomas, M., Metzger, R., Schneider, P.M., et al. (2005). Identification of metastasis-associated receptor tyrosine kinases in non-small cell lung cancer. Cancer Res. *65*, 1778–1782.

Musolino, A., Naldi, N., Bortesi, B., Pezzuolo, D., Capelletti, M., Missale, G., Laccabue, D., Zerbini, A., Camisa, R., Bisagni, G., et al. (2008). Immunoglobulin G fragment C receptor polymorphisms and clinical efficacy of trastuzumab-based therapy in patients with HER-2/neu-positive metastatic breast cancer. J. Clin. Oncol. *26*, 1789–1796.

Narayan, M., Wilken, J.A., Harris, L.N., Baron, A.T., Kimbler, K.D., and Maihle, N.J. (2009). Trastuzumab-induced HER reprogramming in "resistant" breast carcinoma cells. Cancer Res. *69*, 2191–2194.

Nonagase, Y., Yonesaka, K., Kawakami, H., Watanabe, S., Haratani, K., Takahama, T., Takegawa, N., Ueda, H., Tanizaki, J., Hayashi, H., et al. (2016). Heregulin-expressing HER2-positive breast and gastric cancer exhibited heterogeneous susceptibility to the anti-HER2 agents lapatinib, trastuzumab and T-DM1. Oncotarget *7*, 84860–84871.

Ocana, A., Vera-Badillo, F., Seruga, B., Templeton, A., Pandiella, A., and Amir, E. (2013). HER3 overexpression and survival in solid tumors: a meta-analysis. J. Natl. Cancer Inst. *105*, 266–273.

Paterson, B.M., Roselt, P., Denoyer, D., Cullinane, C., Binns, D., Noonan, W., Jeffery, C.M., Price, R.I., White, J.M., Hicks, R.J., and Donnelly, P.S. (2014). PET imaging of tumours with a 64Cu labeled macrobicyclic cage amine ligand tethered to Tyr3-octreotate. Dalton Trans. *43*, 1386–1396.

Paz-Arez, L., Serwatowski, P., Szczęsna, A., Von Pawel, J., Toschi, L., Tibor, C., Morabito, A., Zhang, L., Shuster, D., Chen, S., et al. (2017). P3.02b-045 patritumab plus erlotinib in EGFR wild-type advanced non-small cell lung cancer (NSCLC): part a results of HER3-lung study. J. Thorac. Oncol. *12*, S1214–S1215.

Pradeep, S., Kim, Seung W., Wu, Sherry Y., Nishimura, M., Chaluvally-Raghavan, P., Miyake, T., Pecot, Chad V., Kim, S.-J., Choi, Hyun J., Bischoff, Farideh Z., et al. (2014). Hematogenous metastasis of ovarian cancer: rethinking mode of spread. Cancer Cell *26*, 77–91.

Reynolds, K.L., Juric, D., Baselga, J., Alsina, M., Tabernero, J., Bedard, P.L., Graham, D.M., Gonzalez-Angulo, A.M., Garrido-Laguna, I., Sharma, S., et al. (2014). A phase 1 study of LJM716 in patients with esophageal squamous cell carcinoma, head and neck cancer, or HER2-overexpressing metastatic breast or gastric cancer. J. Clin. Oncol. *32*, 2517.

Retter, I., Althaus, H.H., Münch, R., and Müller, W. (2005). VBASE2, an integrative V gene database. Nucleic Acids Res. *33*, 671–674.

Ritter, C.A., Perez-Torres, M., Rinehart, C., Guix, M., Dugger, T., Engelman, J.A., and Arteaga, C.L. (2007). Human breast cancer cells selected for resistance to trastuzumab in vivo overexpress epidermal growth factor receptor and ErbB ligands and remain dependent on the ErbB receptor network. Clin. Cancer Res. *13*, 4909–4919.

Saunus, J.M., Quinn, M.C., Patch, A.M., Pearson, J.V., Bailey, P.J., Nones, K., McCart Reed, A.E., Miller, D., Wilson, P.J., Al-Ejeh, F., et al. (2015). Integrated genomic and transcriptomic analysis of human brain metastases identifies alterations of potential clinical significance. J. Pathol. *237*, 363–378.

Schaefer, G., Haber, L., Crocker, L.M., Shia, S., Shao, L., Dowbenko, D., Totpal, K., Wong, A., Lee, C.V., Stawicki, S., et al. (2011). A two-in-one antibody against HER3 and EGFR has superior inhibitory activity compared with monospecific antibodies. Cancer Cell *20*, 472–486.

Schoeberl, B., Faber, A.C., Li, D., Liang, M.C., Crosby, K., Onsum, M., Burenkova, O., Pace, E., Walton, Z., Nie, L., et al. (2010). An ErbB3 antibody, MM-121, is active in cancers with ligand-dependent activation. Cancer Res. *70*, 2485–2494.

Schoeberl, B., Pace, E.A., Fitzgerald, J.B., Harms, B.D., Xu, L., Nie, L., Linggi, B., Kalra, A., Paragas, V., Bukhalid, R., et al. (2009). Therapeutically targeting ErbB3: a key node in ligand-induced activation of the ErbB receptor-PI3K axis. Sci. Signal. *2*, ra31.

Sequist, L.V., Lopez-Chavez, A., Doebele, R.C., Gray, J.E., Harb, W.A., Modiano, M.R., Jackman, D.M., Baggstrom, M.Q., Atmaca, A., Felip, E., et al. (2014). A randomized phase 2 trial of MM-121, a fully human monoclonal antibody targeting ErbB3, in combination with erlotinib in EGFR wild-type NSCLC patients. J. Clin. Oncol. *32*, 8051.

Sergina, N.V., Rausch, M., Wang, D., Blair, J., Hann, B., Shokat, K.M., and Moasser, M.M. (2007). Escape from HER-family tyrosine kinase inhibitor therapy by the kinase-inactive HER3. Nature *445*, 437–441.

Shames, D.S., Carbon, J., Walter, K., Jubb, A.M., Kozlowski, C., Januario, T., Do, A., Fu, L., Xiao, Y., Raja, R., et al. (2013). High heregulin expression is associated with activated HER3 and may define an actionable biomarker in patients with squamous cell carcinomas of the head and neck. PLoS One *8*, e56765.

Sheng, Q., Liu, X., Fleming, E., Yuan, K., Piao, H., Chen, J., Moustafa, Z., Thomas, R.K., Greulich, H., Schinzel, A., et al. (2010). An activated ErbB3/NRG1 autocrine loop supports in vivo proliferation in ovarian cancer cells. Cancer Cell *17*, 298–310.

Sliwkowski, M.X., Schaefer, G., Akita, R.W., Lofgren, J.A., Fitzpatrick, V.D., Nuijens, A., Fendly, B.M., Cerione, R.A., Vandlen, R.L., and Carraway, K.L., 3rd (1994). Coexpression of erbB2 and erbB3 proteins reconstitutes a high affinity receptor for heregulin. J. Biol. Chem. *269*, 14661–14665.

Svergun, D.I. (1992). Determination of the regularization parameter in indirect-transform methods using perceptual criteria. J. Appl. Crystallogr. *25*, 495–503.

Wilson, T.R., Fridlyand, J., Yan, Y., Penuel, E., Burton, L., Chan, E., Peng, J., Lin, E., Wang, Y., Sosman, J., et al. (2012). Widespread potential for growth-factor-driven resistance to anticancer kinase inhibitors. Nature *487*, 505–509.

Wilson, T.R., Lee, D.Y., Berry, L., Shames, D.S., and Settleman, J. (2011). Neuregulin-1-mediated autocrine signaling underlies sensitivity to HER2 kinase inhibitors in a subset of human cancers. Cancer Cell *20*, 158–172.

Yarden, Y., and Pines, G. (2012). The ERBB network: at last, cancer therapy meets systems biology. Nat. Rev. Cancer *12*, 553–563.

Yonesaka, K., Hirotani, K., von Pawel, J., Dediu, M., Chen, S., Copigneaux, C., and Nakagawa, K. (2017). Circulating heregulin level is associated with the efficacy of patritumab combined with erlotinib in patients with non-small cell lung cancer. Lung Cancer *105*, 1–6.

Zhou, H., Zha, Z., Liu, Y., Zhang, H., Zhu, J., Hu, S., Shen, G., Cheng, L., Niu, L., Greene, M.I., et al. (2011). Structural insights into the down-regulation of overexpressed p185her2/neu protein of transformed cells by the antibody chA21. J. Biol. Chem. *286*, 31676–31683.

STAR★METHODS

KEY RESOURCES TABLE

REAGENT or RESOURCE	SOURCE	IDENTIFIER
Antibodies		
Anti-HER2xHER3 bispecific antibody (PB4188)	This paper	N/A
Low fucosylated variant of anti-HER2xHER3 bispecific antibody ($PB4188^{LF}$)	This paper	N/A
CH2 double mutant variant (L235G /G236R) of anti-HER2xHER3 bispecific antibody ($PB4188^{DM}$)	This paper	N/A
Anti-HER2 monoclonal antibody (trastuzumab)	Roche	N/A
Anti-HER2 monoclonal antibody (pertuzumab*)	This paper	N/A
Anti-HER3 monoclonal antibody PG3178	This paper	N/A
Anti-HER3 monoclonal antibody (MM-121*)	This paper	N/A
Anti-HER3 monoclonal antibody (AMG888*)	This paper	N/A
Anti-HER3 monoclonal antibody (LJM-716*)	This paper	N/A
Anti-HER2/HER3 bispecific antibody (MM-111*)	This paper	N/A
Trastuzumab emtansine (T-DM1)	Roche	N/A
Anti-HER2xTetanus toxoid bispecific antibody (control)	This paper	N/A
Anti-Tetanus toxoid monospecific antibody (negative control)	This paper	N/A
Anti-EGFR monoclonal antibody (cetuximab)	Eli Lilly	N/A
Anti-HER2/EGFR tyrosine kinase inhibitor (lapatinib)	Selleckchem	Cat#S2111
Anti-human HER2 mouse monoclonal antibody	R&D Systems	Cat#MAB1129; RRID: AB_2099244
Anti-human HER3 mouse monoclonal antibody	R&D Systems	Cat#MAB3481; RRID:AB_358278
Phospho-Akt (Ser 473) rabbit monoclonal antibody	Cell Signaling Technology	Cat#4060; RRID:AB_2315049
Total Akt rabbit monoclonal antibody	Cell Signaling Technology	Cat#4691; RRID:AB_915783
Phospho-HER2 (Tyr 1221/1222) rabbit monoclonal antibody	Cell Signaling Technology	Cat#2243; RRID:AB_490899
Total HER2 polyclonal antibody	Cell Signaling Technology	Cat#2242; RRID:AB_10694349
Phospho-HER3 (Tyr 1289) rabbit monoclonal antibody	Cell Signaling Technology	Cat#4791; RRID:AB_2099709
Total HER3 rabbit monoclonal antibody	Cell Signaling Technology	Cat#4754; RRID:AB_10691324
Phospho-ERK1/2 (Thr 202/Tyr 204) rabbit monoclonal antibody	Cell Signaling Technology	Cat#4377; RRID:AB_331775
Total ERK1/2 (Thr 202/Tyr 204) rabbit monoclonal antibody	Cell Signaling Technology	Cat#4695; RRID:AB_390779
Phospho-S6 ribosomal protein (Ser 235/236) polyclonal antibody	Cell Signaling Technology	Cat#2211; RRID:AB_331679

(*Continued on next page*)

Continued

REAGENT or RESOURCE	SOURCE	IDENTIFIER
Total S6 ribosomal protein rabbit monoclonal antibody	Cell Signaling Technology	Cat#2217; RRID:AB_331355
Anti-rabbit IgG HRP-linked antibody	Cell Signaling Technology	Cat#7074; RRID:AB_2099233
Bacterial and Virus Strains		
E.coli TG-1	Lucigen	Cat#60502-1
E.coli XL1-Blue	Stratagene	Cat#200249
VCS-M13 helper phage	Stratagene	Cat#200251
Biological Samples		
ST1360B PDX	Minerva	https://doi.org/10.1158/1535-7163.TARG-15-C74
OV-10-0050 PDX	WuXi	https://doi.org/10.1158/1538-7445.AM2016-4759
Chemicals, Peptides, and Recombinant Proteins		
Human NRG1-beta 1/HRG1-beta 1 EGF-like domain	R&D Systems	Cat#396-HB
Human NRG1-beta 1/HRG1-beta 1 EGF-like domain	Prospec Bio	Cat#Cyt-733
Human EGF	DiscoverX	Cat#92-1113
Human HER2 Fc chimera	R&D Systems	Cat#1129-ER
Human HER3 Fc chimera	R&D Systems	Cat#348-RB
Human HER4 Fc chimera	R&D Systems	Cat#1131-ER
Human EGFR Fc chimera	R&D Systems	Cat#344-ER
Human HER2 ectodomain	Bender MedSystems	Cat#362
Critical Commercial Assays		
Alamar Blue™	Invitrogen	Cat#DAL1100
Click-iT™ EdU AlexaFluor™ 488 Imaging Kit	Life Technologies	Cat#C10337
PathScan® RTK Signaling Antibody Array Kit	Cell Signaling	Cat#7949
PathScan® Intracellular Signaling Array Kit	Cell Signaling	Cat#7323
PathHunter® U2OS Dimerization Cell Line	DiscoverX	N/A
Human IgG ELISA	ZeptoMetrix	Cat# 0801182
VeraTag® Assay	Monogram Biosciences	N/A
Cell Signaling Multiplex Assays	Millipore	Cat# 48-618MAG, 46-645MAG, 46-645M-1K
ADCC Reporter Bioassay	Promega	Cat#G7011, G9790, G7941
Epitope mapping	Integral Molecular	N/A
Deposited Data		
HER2-ECD:MF3958 structure	This paper	PDB: 5O4G
HER3-ECD:MF3178 structure	This paper	PDB: 5O4O, 5O7P
Experimental Models: Cell Lines		
Human: JIMT-1	DSMZ	Cat#ACC-589; RRID:CVCL_2077
Human: SKBR-3	ATCC	Cat#HTB-30; RRID:CVCL_0033
Human: BT-474	DMSZ	Cat#ACC-64; RRID:CVCL_0179
Human: MCF-7	DMSZ	Cat#ACC-115; RRID:CVCL_0031
Human: MDA-MB-468	Cell Line Service	N/A

(*Continued on next page*)

Continued

REAGENT or RESOURCE	SOURCE	IDENTIFIER
Human: MDA-MB-175	ATCC	Cat#HTB-25; RRID:CVCL_1400
Human: MDA-MB-453	ATCC	Cat#HTB-131; RRID:CVCL_0418
Human: MDA-MB-361	ATCC	Cat#HTB-27; RRID:CVCL_0620
Human: ZR-75-1	ATCC	Cat#CRL-1500; RRID:CVCL_0588
Human stem cell-derived cardiomyocytes	Pluriomics BV	N/A
Human: N87	ATCC	Cat#CRL-5822; RRID:CVCL_1603
Human: BxPC-3	ATCC	Cat#CRL-1687; RRID:CVCL_0186
Human: BxPC-3-luc2	Taconic	N/A
Human: K562	DSMZ	Cat#ACC-10; RRID:CVCL_0004
Human: K562 stably overexpressing HER3	This paper	N/A
Human: GnTI-deficient HEK293-EBNA	UPE	N/A
Human: FreeStyle™ 293-F	Invitrogen	Cat#R790-07
Human: HEK293T	ATCC	Cat#CRL-11268; RRID:CVCL_1926
Mouse: L929	Sigma-Aldrich	Cat# 85011425; RRID:CVCL_0462
Hamster: CHO-K1	DSMZ	Cat#ACC-110; RRID:CVCL_0214
Experimental Models: Organisms/Strains		
Mouse: CB.17 SCID	ARC	RRID:IMSR_ARC:SCID
	Taconic	RRID:IMSR_TAC:cb17sc
	Charles River	RRID:IMSR_CRL:236
Mouse: NMRI nude mice	Janvier Labs	https://www.janvier-labs.com/rodent-research-models-services/research-models/per-species/mutant-mice/product/nmri-nu.html
Mouse: BALB/c nude mice	Shanghai Sino-British SIPPR/BK Laboratory Animal Co.	Animal certificate number: 2008001664095
Mouse: C57/BL6 mice	Taconic	N/A
Recombinant DNA		
pcDNA3.1	Invitrogen	Cat#V790-20
pVAX1 vector	Invitrogen	Cat#V260-20
pDisplay vector	Invitrogen	Cat#V660-20
pcDNA3.1-HER2	This paper	N/A
pVAX1 HER2-ECD	This paper	N/A
pVAX1 HER3-ECD	This paper	N/A
Software and Algorithms		
Prism Software v6.0	GraphPad Software	www.graphpad.com
Image Studio Software	LI-COR Biosciences	https://www.licor.com/bio/products/software/image_studio/
VBASE2	Retter et al., 2005	http://www.vbase2.org/
Horos	Horos Project	http://www.horosproject.org/
IMOSFLM	Battye et al., 2011	http://www.mrc-lmb.cam.ac.uk/harry/imosflm/ver721/introduction.html
AIMLESS	Evans and Murshudov, 2013	www.ccp4.ac.uk/html/aimless.html
PHASER MR	McCoy et al., 2007	www.ccp4.ac.uk/html/phaser.html

(*Continued on next page*)

Continued

REAGENT or RESOURCE	SOURCE	IDENTIFIER
COOT	Emsley et al., 2010	https://www2.mrc-lmb.cam.ac.uk/Personal/pemsley/coot/
PHENIX	Adams et al., 2010	https://www.phenix-online.org/
PYMOL v1.5.0	Schrödinger	http://pymol.org
PRIMUS	Konarev et al., 2003	https://www.embl-hamburg.de/biosaxs/primus.html
GNOM	Svergun, 1992	https://www.embl-hamburg.de/biosaxs/gnom.html
DAMMIF	Franke and Svergun, 2009	https://www.embl-hamburg.de/biosaxs/dammif.html

CONTACT FOR REAGENT AND RESOURCE SHARING

Further information and requests for resources and reagents should be directed to and will be fulfilled by the Lead Contact, Mark Throsby (m.thosby@merus.nl).

EXPERIMENTAL MODEL AND SUBJECT DETAILS

Mouse Models

All procedures were approved by the Institutional Animal Care and Use Committee (IACUC) of the University of Queensland (for studies carried out under the direction of Clarity Pharmaceuticals), Taconic, Charles River Laboratories, University of Copenhagen (for studies carried out under the direction of Minerva Imaging) and WuXi AppTec, and all experiments conformed to the relevant regulatory standards. Female CB.17 SCID mice were obtained from the Animal Resource Centre (ARC) (biodistribution study), from Taconic (BxPC-3 model) and from Charles River Laboratories (JIMT-1 model). Female NMRI nude mice were obtained from Janvier Labs. Female BALB/c Nude-nu/nu mice (BALB/c/BKL background) were obtained from Shanghai Sino-British SIPPR/BK Laboratory Animal Co., Ltd.

Cell Lines

Human Cell Lines

The following human cell lines derive from breast tissue of female breast cancer patients: MCF-7, MDA-MB-468, MDA-MB-175, MDA-MB-453, MDA-MB-361, ZR-75-1, JIMT-1, BT-474, and SKBR-3. The N87 cell line derives from gastric carcinoma tissue of a male patient. The BxPC-3 cell line derives from pancreatic adenocarcinoma of a female patient. The Bioware® Cell Line BxPc-3-luc2 was established by lentiviral transduction of a vector delivering the firefly luciferase-2 (luc2) gene under the control of human ubiquitin C promoter (Taconic). The human K-562 cell line derives from bone marrow tissue of a female patient with chronic myelogenous leukemia (CML). The human stem cell-derived cardiomyocytes are ventricular cardiomyocytes that have been differentiated from human-induced pluripotent stem cells of unknown sex. Human embryonic kidney (HEK) 293T cells (ATCC) were used for FACS and epitope mapping studies. FreeStyle™ 293-F cells (Invitrogen) were used to produce full-length IgGs and Fab fragments. N-acetylglucoaminyltransferase I (GnTI)-deficient HEK293-Epstein-Barr virus nuclear antigen (EBNA) cells (U-Protein Express) were used to produce receptor ECDs for crystallography and SAXS experiments.

All cell lines were maintained at 37°C in a humidified atmosphere at 5% CO_2, unless otherwise indicated in figure legends or method details. SKBR-3 cells were cultured in DMEM F/12 medium (Life Technologies, Cat#21331-020) supplemented with L-glutamine (Invitrogen, Cat#25030-024) and 10% heat-inactivated fetal bovine serum (FBS) (HyClone™, GE Healthcare, Cat#V30180.3). BxPC-3-luc2 and N87 cells were cultured in RPMI-1640 (Invitrogen, Cat#21875-034) supplemented with 10% heat-inactivated FBS. MCF-7 cells were cultured in RPMI-1640 (Invitrogen, Cat#21875-034) supplemented with 100 μM MEM Non-Essential Amino Acids (NEAA, Invitrogen, Cat#11140-035), 1 mM sodium pyruvate (Invitrogen, Cat#11360-039), 4 μg/ml insulin (Invitrogen, Cat#12585-014) and 10% heat-inactivated FBS. JIMT-1 cells were cultured in DMEM (Invitrogen, Cat#41966-029) and 10% heat-inactivated FBS. FreeStyle™ 293-F cells were maintained in 293 FreeStyle expression medium (Invitrogen, Cat#12338026).

Other Cell Lines

The CHO-K1 cell line derives from ovary biopsy tissue of a female adult Chinese hamster and was maintained in DMEM F/12 medium (Life Technologies, Cat#21331-020) supplemented with 10% FBS (HyClone™, GE Healthcare, Cat#V30180.3) and L-glutamine (Invitrogen, Cat#25030-024), at 37°C in a humidified atmosphere at 5% CO_2. The mouse L929 fibroblast cell line derives from adipose tissue from a male C3H/An mouse and was maintained in RPMI-1640 (Invitrogen, Cat#21875-034) supplemented with 10% heat-inactivated FBS (HyClone™, GE Healthcare, Cat#V30180.3).

METHOD DETAILS

Recombinant Proteins and Constructs

Recombinant Fc-tagged human EGFR, HER2, HER3 and HER4 extracellular domain (ECD) proteins were purchased from R&D Systems (Cat# 344-ER, 1129-ER, 348-RB, 1131-ER). Recombinant human NRG1-beta 1/HRG1-beta 1 EGF-like domain protein was purchased from R&D Systems (Cat#396-HB) and Prospec Bio (Cat#Cyt-733). Recombinant human EGF was purchased from DiscoverX (Cat#92-1113). Human NRG1-beta 1/HRG1-beta 1 EGF-like domain will hereinafter be referred to as HRG. Recombinant human HER2 ectodomain protein was provided by Bender MedSystems. Constructs expressing human, cynomolgus, rat or mouse HER2 and HER3 ECDs were generated in pVAX1 vector (Invitrogen, Cat#V260-20) for DNA immunizations, and in pDisplay vector (Invitrogen, Cat#V660-20) for cell line transfections. All constructs were sequence verified. VH and VL sequences from anti-HER2 monospecific antibody (mAb) pertuzumab (P), anti-HER3 mAbs MM-121, AMG888 and LJM-716, and anti-HER2/HER3 bispecific antibody MM-111 were extracted from published patents, synthesized and recloned in the IgG1 backbone vector to use them as reference antibodies. These reference antibodies are marked with an asterisk in the manuscript. Trastuzumab (T) was purchased from hospital formularies. The equimolar combination of trastuzumab plus pertuzumab* is described throughout the manuscript as T+P*.

Immunizations, Phage Library Generation and Selection

C57/BL6 mice were immunized every 2 weeks with the following material: L929 cells expressing HER2 or HER3 (2×10^6 cells); Fc-HER2 or Fc-HER3 (20 μg/mouse in Titermax Gold, R&D Systems); or DNA vaccination with pVax-HER2 or pVax-HER3. Sera were screened for binding to transfected HEK293T-HER2 or -HER3 cells and for recombinant HER2 and HER3 proteins in ELISA. Common light chain phage libraries were constructed from immunized mouse material as previously described (de Kruif et al., 2009). Briefly, from each individual mouse, RNA was isolated, cDNA was synthesized and VH-family-specific PCRs were performed. Subsequently, all VH family PCR products per mouse were purified, digested and ligated in a phage-display vector containing the common light chain (Table S3) to generate a phage library containing mouse-human chimeric Fab domains. All phage libraries contained $>10^6$ clones with an insert frequency of >85%. Antibody fragments were selected using antibody phage display libraries. Immunized libraries and synthetic common light chian Fab libraries (de Kruif et al., 1995) were used for selections. Phage libraries were rescued with VCS-M13 helper phage (Stratagene) and selected for two rounds in immunotubes (Nunc) coated with recombinant protein. Positive phage clones binding HER2 or HER3 were then identified by FACS for binding to the breast cancer cell line BT-474. The VH genes of all HER2 and HER3 specific clones were sequenced. VH gene rearrangements were established with VBASE2 software to identify unique clones. All HER2 unique clones were then tested in phage format for binding in FACS to HEK293T cells (negative control), HEK293T cells transiently transfected with HER2, and BT-474 cells. HER3-specific phage clones were selected on K562 cells, K562 cells stably overexpressing HER3, and BT-474 cells. VH genes of unique antibodies, as judged by VH gene sequence and some sequence variants thereof, derived from the immunized mouse phage libraries were cloned in the backbone IgG1 vector as described (de Kruif et al., 2009). IgGs were produced in transiently transfected Freestyle™ 293-F (Invitrogen) cells according to manufacturer's instructions. Bispecific antibodies were generated with a mutated IgG1 Fc variant region known as DEKK (De Nardis et al., 2017) to ensure efficient hetero-dimerization and formation of a bispecific antibody. This technology uses charge-based point mutations (L351D/L368E and L351K/T366K) in the CH3 region to allow efficient pairing of two different heavy chain molecules. Antibodies were purified using protein A batch purification (Pierce). Antibodies were characterized based on their affinity in antigen titration ELISA. The panel of anti-HER2 and HER3 antibodies was grouped or "binned" based on their binding to CHO-K1 cells transiently transfected with an HER2 or HER3 ECD derived from various species (human, cynomolgus, mouse, rat, chicken) or with HER2 or HER3 domain-swapped chimeric constructs. Chimeric domain-swapped constructs for HER2 and HER3 were generated by swapping human domains I to IV with one of the chicken (HER2) or rat (HER3) orthologues.

Humanization

Anti-HER2 mouse Fab MF3004 variant was humanized by CDR grafting technology, and its immunogenicity potential further reduced by T cell epitope elimination in silico (Lonza). A total of 7 humanized/de-immunized variant sequences of MF3004 were expressed, validated and characterized *in vitro* as monoclonal antibody, as well as in bispecific format with anti-HER3 human Fab MF3178. Based on production, integrity, stability and functionality, a variant of MF3004 was chosen as the optimal humanized variant of the VH to be used in a bispecific format with MF3178. This variant was renamed MF3958. The bispecific HER2xHER3 combination MF3958xMF3178 resulted in PB4188.

Cell Line Proliferation Assays

Proliferation assay media for the different cell lines were as follows: RPMI-1640 (Invitrogen, Cat#21875-034), 0.05% BSA (Sigma-Aldrich, Cat# A9576), 10 μg/ml Holo-transferrin (Sigma-Aldrich, Cat#T1283), 1 mM sodium pyruvate (Invitrogen, Cat#11360-039), MEM NEAA (Invitrogen, Cat#11140-035) for MCF-7 cells; DMEM (Invitrogen, Cat#41966-029), 0.05% BSA (Sigma-Aldrich, Cat#A9576) for JIMT-1; DMEM/F-12 (Life Technologies, Cat#21331-020), 2 mM L-glutamine (Invitrogen, Cat#25030-024), 0.05% BSA, 10 μg/ml Holo-transferrin for SKBR-3 cells; RPMI-1640, 0.05% BSA, 10 μg/ml Holo-transferrin for N87 cells.

Proliferation Inhibition Assays

Conventional Plate-based Proliferation Assays

Subconfluent cell cultures were harvested in assay medium and resuspended in medium containing recombinant human HRG (R&D Systems, Cat#396-HB). Dilution series of antibodies were added to the cells in a total volume of 100 μl in 96-well black-bottom plates (ABgene, Cat#AB-0932). Cells were cultivated for 3-5 days before Alamar Blue™ (Invitrogen, Cat#DAL1100) was added according to the manufacturer's instructions and incubated at 37°C for an additional 6 or 24 hr. Fluorescence was measured at 550 nm excitation and 590 nm emission wavelengths (BioTek Synergy 2 Multi-Mode Microplate Reader).

Suspension Proliferation Assays in Agar Plates

100 μl of a soft agar bottom layer (0.6% final concentration in complete medium) was added per well of 96-well plates and left to solidify. 50 μl of a soft agar top layer (0.4% final concentration) containing 10,000 JIMT-1 cells were then added per well and incubated for 24 hours at normal culture conditions. Titration of antibodies in DMEM medium were added and incubated for 8 days. Alamar Blue™ (Invitrogen, Cat#DAL1100) was then added to the wells; after incubation for 3-5 hr at 37°C, fluorescence intensity was determined (excitation 560 nm; emission 590 nm) (BioTek Synergy 2 Multi-Mode Microplate Reader).

3D Phenotypic Assay

SKBR-3 or BT474 cells were seeded in 15 μl basement membrane protein-rich hydrogel (OcellO) per well of a 384-well plate (Greiner Bio-One, Cat#781091). 24 hr later, antibodies diluted in culture medium (concentration ranges from 0.003 up to 1 μg/ml) were added in quadruplicate in the absence or presence of 12.5 nM HRG (R&D Systems, Cat#396-HB). Cells were incubated for 7 days at 37°C, 5% CO_2. Cells were then fixed with 3% formaldehyde (Sigma-Aldrich), permeabilized with 0.2% Triton-X100 (Sigma-Aldrich) and stained with 0.25 μm rhodamine-phalloidin (Sigma-Aldrich) and 0.1% Hoechst 33258 (Sigma-Aldrich) in PBS at 4°C for 16 hr. After staining, the plate was washed in PBS and covered with a Greiner SilverSeal (Greiner Bio-One). Fluorescent images were taken at different levels through the gel (Z-stack) using a Molecular Devices Image Express automated inverted fluorescence microscope (Molecular Devices) with a 4× Olympus objective. Ominer image analysis software (OcellO) was used to reconstruct 3D image stacks. A variety of morphological features were measured in the different fluorescence channels (800 in total). Only features that differed between medium and HRG treatments were selected for analysis. Single parameter analyses were performed and t-tests were used to compare treatments to medium.

Cell Cycle Analysis in HRG-stimulated Cell Lines

MCF-7, JIMT-1 and SKBR-3 cells were seeded into 24-well plates in 1 ml assay medium and incubated overnight at 37°C, 5% CO_2. 24 hr later antibodies were added in the presence of HRG (0.125 or 12.5 nM) (R&D Systems, Cat#396-HB) and incubated for 24 (for JIMT-1 or SKBR-3 cells) or 48 hr (for MCF-7 cells). Cells were then harvested and stained with the Click-iT 5-ethynyl-2′-deoxyuridine (EdU) AlexaFluor488 kit (LifeTechnologies) according to the manufacturer's instructions. 30 minutes prior to analysis by flow cytometry, cells were incubated with 200 nM FxCycle™ Far Red Stain (LifeTechnologies, Cat#F10348) and 100 μg/ml RNAse A (LifeTechnologies, Cat#12091-039). Data were analyzed by gating single cells on an FSC-width vs FSC-height scatter plot, and subgating the G0/G1, S and G2M phases of the cell cycle on an APC vs AlexaFluor488 scatter plot; the $EdU^{neg}APC^{low}$ population was considered as being in G0/G1 phase, EdU^{pos} in S phase, and $EdU^{neg}APC^{high}$ in G2M phase (FlowJo, LLC). Data were represented as the proliferation index, calculated by dividing the percentage of cells in the S and G2/M phases by the percentage of cells in the G0/G1 phase.

PathHunter Dimerization Assay

Heterodimerization assays for EGFR/HER2, HER2/HER3 and HER2/HER4 were performed with PB4188, AMG888*, trastuzumab and pertuzumab*. A heterodimerization assay for EGFR/HER3 was performed with PB4188, cetuximab (Roche), AMG888* and pertuzumab*. The anti-tetanus toxoid mAb was included as negative control in all the assays. Antibodies were assayed in quadruplicates at a maximum concentration of 100 nM. Antibodies were pre-incubated for 3 hr with reporter cells expressing different combinations of EGFR, HER2, HER3 and HER4, followed by stimulation with the agonistic ligands. Recombinant human EGF (10 ng/ml) (DiscoverX) was used for induction of EGFR/HER2 dimers and recombinant human HRG (Prospec Bio) for HER2/HER3 (30 ng/ml), HER2/HER4 (30 ng/ml) and EGFR/HER3 (230 ng/ml) dimers. Heterodimerization was determined by measuring β-galactosidase-based fluorescence 16 hr later (EnVision luminometer, PerkinElmer).

In Vitro Cardiomyocyte Viability Assay

Human stem cell-derived cardiomyocytes (Pluriomics BV) were seeded at a density of 20,000/well in white flat-bottom assay plates (Corning, Cat#655098). On day 5 of culture, the medium was replaced with glucose- and galactose-free culture medium supplemented with 12.5 nM HRG (R&D systems, Cat#396-HB). On day 7, antibodies were added at 68 or 210 nM in combination with 3 μM doxorubicin (Pluriomics BV). Cell viability was assayed on day 9 by measuring cellular ATP using the CellTiter-Glo assay (Promega, Cat#G7571).

Phosphorylation Assays

PathScan Array Analysis

Cells in logarithmic growth phase were harvested and seeded in 6-well plates in starvation medium and incubated overnight. The next day, antibodies were added to a final concentration of 5 nM, incubated for one hour at 37°C, and HRG (R&D systems, Cat#396-HB) was added to a final concentration of 12.5 nM (100 ng/ml). After 24 hr incubation, plates were placed on ice and cells were washed

twice with cold PBS. Subsequently, cells were washed and lysed in cell lysis buffer (Cell Signaling, Cat#9803) for a minimum of 30 minutes on ice. Protein concentrations were measured using the Pierce™ BCA protein assay kit (Invitrogen, Cat#23235) and adjusted to 2 mg/ml with lysis buffer. PathScan RTK Signaling Antibody Arrays (Cell Signaling, Cat#7949) or PathScan Intracellular Signaling Antibody Arrays (Cell Signaling, Cat#7744) were used according to the manufacturer's guidelines using 800 μg/ml protein lysate. Slides were allowed to dry before imaging on an Odysey®Clx system (LI-COR Biosciences). Spot fluorescence intensity was calculated using Image Studio Software (LI-COR Biosciences). Data were normalized against signals measured in cells not stimulated with HRG.

Western Blot Analysis

$20x10^6$ N87 cells were seeded in 10 cm dishes in starvation medium. The next day, antibodies were added to a final concentration of 5 nM (PB4188, trastuzumab + pertuzumab*) or 10 μM (lapatinib, Selleckhem Cat#S2111), and cells were incubated for one hour. HRG (R&D Systems, Cat#396-HB) was then added to a final concentration of 12.5 nM. After 1, 3, 6 or 24 hr, dishes were placed on ice, washed twice with cold PBS and cells were lysed in RIPA lysis buffer (Cell Signaling Technology, Cat#9806) supplemented with Protease Inhibitor Cocktail (Cell Signaling Technology, Cat#5871). 30 μg of protein lysate was analyzed by Western blot using the following primary rabbit antibodies (Cell Signaling Technology): Phospho-Akt (ser 473, Cat#4060), Total Akt (Cat#4691), Phospho-HER2 (Tyr 1221/1222, Cat#2243), Total HER2 (Cat#2242), Phospho-HER3 (Tyr 1289, Cat#4791), Total HER3 (Cat#4754), Phospho-ERK1/2 (Thr 202/Tyr 204, Cat#4377), Total ERK1/2 (Cat#4695), Phospho-S6 RP (Ser 235/236, Cat#2211), and Total S6 RP (Cat#2217). Protein expression levels were detected with HRP-conjugated goat anti-rabbit IgG (Cat#7074) in combination with enhanced chemiluminescence with X-ray films (Amersham).

Cell Surface Binding Measured by FACS

FACS was performed on the following breast cancer cell lines that are reported to express varying levels of surface HER2: MCF-7 ($HER2^+$), MDA-MB-468 ($HER2^+$), MDA-MB-175 ($HER2^+$), MDA-MB-453 ($HER2^{++}$), MDA-MB-361 ($HER2^{++}$), ZR-75-1 ($HER2^{++}$), JIMT-1 ($HER2^{+++}$), BT-474 ($HER2^{+++}$), and SKBR-3 ($HER2^{+++}$). Cells in exponential growth were harvested and resuspended in FACS buffer (10^6 cells/ml in PBS, 0.5% BSA, 0.5 mM EDTA). $1\text{-}2x10^5$ cells were stained for 1 hour on ice with 50 μl of primary antibody. After washing, bound antibodies were detected with PE-labelled goat anti-human IgG (Invitrogen, Cat#H10104). Cells were analyzed by FACS for median fluorescence intensity in the PE channel (FACSCanto Flow cytometer, BD Biosciences).

Affinity Determination

Antibodies were radiolabeled with ^{125}I using IODO-GEN® Pierce Precoated Iodonation Tubes (Thermo Scientific, Cat#28601) according to the manufacturer's instructions. Radiolabeled IgGs were diluted to an activity of $\sim$1-2 x 10^8 cpm/ml in 25 mM Tris-HCl, 0.4 M NaCl, 0.25% BSA, 5 mM EDTA, 0.05% NaN_3. Flow cytometry analysis of the labeled and non-labeled IgG using BT-474 and SKBR-3 cells showed no or only minor signs of reduction in binding after radiolabeling. Steady state cell affinity measurements were performed by seeding SKBR-3 or BT-474 cells in 96-well plates at 10,000 cells/well. The next day, various concentrations of antibodies were added and incubated at 4°C for 4 hours. Unbound radiolabeled antibodies were washed away and cell-bound radioactivity was measured using a gamma counter (WIZARD2, PerkinElmer). Non-specific binding was measured by adding a receptor-blocking concentration (100-fold excess) of unlabeled antibody. Each condition was tested in triplicate and three independent experiments were performed per antibody. K_D values were calculated based on a non-linear regression model that compensates for non-specific binding (Prism 6.0, GraphPad).

Antibody-dependent Cytotoxicity Assays

Chromium Release Assays

SKBR-3 ($HER2^{+++}$) and MCF-7 ($HER2^+$) target cells were loaded with ^{51}Cr (Amersham) and incubated with an increasing concentration of antibody. PBMC fractions isolated from healthy donors were used as effector cells in a 200 μl reaction in RPMI 1640 + 10% heat-inactivated FBS. Cells were incubated for 4 hours, and lysis was estimated by measuring radioactivity in the supernatant using a gamma counter to measure counts per minute (cpm) (WIZARD2, PerkinElmer). Percentage of specific lysis was calculated as follows: (experimental cpm − basal cpm) / (maximal cpm − basal cpm) × 100, with maximal lysis determined in the presence of 5% Triton X-100 and basal lysis in the absence of antibody and effectors.

Reporter Assays

The ADCC reporter gene assay from Promega was used and adapted to 384-well plate format. Briefly, SKBR-3 target cells were seeded at a density of 1000 cells/well in 30 μl assay medium (RPMI with 4% low IgG serum), 20-24 hr before the bioassay. Culture medium was then removed and 10 μl of serially diluted antibodies were added to the wells in duplicate and combined with 5 μl of either the V158 or F158 FcγRIIIa variant Jurkat reporter cell lines. Cells were incubated for 6 hours at 37°C, then 15 μl Bio-Glo luciferase substrate was added per well, incubated for 5 minutes and luminescence was detected on a plate reader (BioTek Synergy 2 Multi-Mode Microplate Reader).

Internalization Assay

Purified antibodies were labelled with a pH sensor dye with a succinimidyl ester reactive group (Promega, Cat#CS1783A01) according to the manufacturer's instructions. SKBR-3 and N87 cells in an exponential growth phase were harvested and seeded in 96-well

plates ($1.5x10^4$ cells per well) in 100 μl assay medium containing 0.125 nM HRG (R&D Systems, Cat#396-HB). After overnight incubation, 20 μl of pH-sensitive dye-labelled antibodies were added to reach a final concentration of 100 nM. After overnight incubation, cells were harvested by collecting non-adherent cells and by trypsinizing adherent cells. Cells were washed with FACS buffer (PBS 0.5% BSA, 0.1% sodium azide) and analyzed by flow cytometry on a FACSCanto Flow cytometer (BD Biosciences). Median fluorescence intensities (MFI) of the PE channel were used to determine the extent of internalization.

Xenograft Studies

BxPC-3 Model

8-10 week old CB.17 SCID female mice (Taconic) were anesthetized and laid on the right side. A 0.5 cm incision was made in the left flank and pancreas and spleen were exteriorized. 1×10^6 BxPC-3-luc2 tumor cells in a volume of 20 μl were injected into the subcapsulary space of the pancreas tail. One week after implantation, bioluminescence imaging (BLI) data were generated. 15 minutes prior to imaging, all the mice received i.p. injections of 150 mg/kg luciferin (D-Luciferin-EF Potassium Salt, Promega, Cat#E6552). BLI was performed once or twice weekly using the left side view. Outlier animals – based on BLI/tumor volume – were removed and the mice were randomly distributed into groups of 7 mice. Treatment was started on experimental day 8. The animals in the antibody treatment group were dosed weekly for 3 consecutive weeks (days 0, 7, 14 and 21) with 30 mg/kg of antibody ($PB4188^{LF}$, trastuzumab + pertuzumab*). At day 0 of treatment, the animals received twice the loading dose, i.e. 60 mg/kg of antibody ($PB4188^{LF}$, trastuzumab + pertuzumab*). The final imaging was carried out on day 31.

Biodistribution Study

Variants of bAb PB4188 (PB11247), anti-HER3 PG3178 (PG6058) and anti-HER2 PG3958 (PG3004) were conjugated to a bifunctional chelator (Paterson et al., 2014). The PB4188 and PG3178 variants were both fully cross-reactive for human and murine HER3. Binding characteristics of the conjugated products were confirmed using flow cytometry-based binding assays. Proteins were then labelled with ^{64}Cu, and CB.17 SCID mice (ARC) bearing JIMT-1 xenografts (467 ± 125 mm^3 across all animals enrolled in the study) were administered the radiolabeled antibodies via tail vein injection. MicroPET/CT images were acquired 24 and 48 hr post-injection. Tumors were then excised and radioactivity was measured in a gamma counter (WIZARD2, PerkinElmer). Results were expressed as percentage injected dose per gram tissue (%ID/g).

JIMT-1 Model

8-week old female CB.17 SCID mice (Charles River) were injected subcutaneously in the right flank with $5x10^6$ JIMT-1 tumor cells (0.2 ml cell suspension harvested from exponentially growing cultures). The tumors were measured twice a week with a caliper in two dimensions to monitor size. Once tumor size had reached ~ 150 mm^3, animals were enrolled in the efficacy study and randomly distributed into groups of 10 mice. Mice received four weekly injections of antibody and tumor size was measured biweekly by caliper.

In the comparative efficacy study, the mice were injected i.p. with vehicle, 2.5 mg/kg $PB4188^{LF}$ or 2.5 mg/kg of the combination of T+P* on days 1, 8, 15 and 22. Tumor volume was measured over time by caliper.

In the pharmacokinetic/pharmacodynamic study, the mice were injected i.p. with vehicle or different doses of $PB4188^{LF}$ (25, 2.5, 0.25, 0.025 and 0.0025 mg/kg) on days 1, 8, 15 and 22. Tumor volume in the treated animals was normalized against vehicle-treated animals on day 24. Serum was obtained 24 hours after the last dose and analyzed for human IgG titers (ZeptoMetrix, Cat# 0801182).

ST1360B Intracranial Model

ST1360B patient-derived xenograft (PDX) tumors were grown subcutaneously in NRMI nude mice (Janvier Labs) and harvested to prepare cell suspension by enzymatic treatment. Then, a new group of NMRI nude mice was anaesthetized by hypnorm/midazolam (1 ml/100 g body weight) and placed in a stereotactic frame (Better Hospital Equipment Corp.). A longitudinal incision was made in the scalp exposing the calvarium. A hole was drilled in the skull 1.5 mm to the right of the sutura saggitalis and 0.5 mm posterior to the bregma using a micro-drill (marathon motor hand piece SDE-BM50S1). 10 μl of the cell suspension (180,000 cells) was injected at a depth of 2–2.5 mm at a rate of 60 nl/sec using a 100 μl syringe with a 25-gauge needle placed in a micro infusion pump (World Precision Instruments, Cat#SGE100RN). Bupivacaine (0.2 mg/100 g body weight, AstraZeneca) and lidocaine (1 mg/100 g body weight, Mylan Hospital) were administrated in the incision site for local anesthesia and the skin was closed with a suture. Mice were monitored until fully recovered from the anesthesia, and at least twice a week after tumor inoculation (weight and clinical signs); more often if clinical signs or weight loss were present. 24 NMRI nude mice were enrolled in the study based on two pathological MR scans showing tumor growth and a tumor volume of 10-20 mm^3. Once mice met the enrolment criteria, animals were randomized into one of three groups so that all groups presented the same mean tumor volume at treatment initiation. Mice were treated i.v. with vehicle (isotonic saline, 5 mg/kg, twice per week), $PB4188^{LF}$ (25 mg/kg, twice per week) or T-DM1 (10 mg/kg, once a week, Roche). Image analysis was performed using Horos (www.horosproject.com). Animals were observed for clinical signs and scored for changes in body weight, behavior or physical appearance. Animals with deteriorating health (clinical score superior to a pre-defined threshold) were euthanized by cervical dislocation.

OV-10-0050

The human ovarian cancer PDX model OV-10-0050 was originally established from a 48-year-old female patient with grade 3 adenocarcinoma of the ovaries. A surgically resected clinical sample was implanted in nude mice (defined as passage 0, P0) and the following serial implantations were defined as P1, P2, etc. P6 tumor tissue was used for this study. BALB/c nude mice were implanted subcutaneously in the right flank with OV-10-0050 P6 tumor slices (~30 mm^3). Treatments were

started on day 30 after tumor implantation when the average tumor size had reached approximately 152 mm^3. 32 tumor-bearing mice were randomized into 4 groups with a stratified randomization method, and each group consisted of 8 tumor-bearing mice. Day 1 was the day of randomization and the day of start of treatment. BALB/c nude mice bearing s.c. OV-10-0050 PDX tumors were treated once per week during 28 days with PBS or $PB4188^{LF}$ (25 mg/kg). Tumor growth was monitored by caliper measurements.

HER Expression and Downstream Phosphorylation

VeraTag Assay

Mice bearing JIMT-1 tumor xenografts (300-400 mm^3) were injected i.p. with vehicle or 25 mg/kg $PB4188^{LF}$ on days 1 and 8. 4 hours after the last dose, tumors were removed and immediately placed in 10% neutral buffered formalin for about 24 hours and then paraffin-embedded. Freshly-cut 5 μm sections were placed on positively charged glass slides (FisherScientific) and analyzed using the VeraTag® Technology (Monogram Biosciences). Briefly, samples were deparaffinized, rehydrated, and antigen retrieval was performed via heat using a pressure cooker (Biocare Medical). Antibody pairs for each VeraTag assay were added, samples illuminated and the released fluorescent VeraTags were detected by capillary electorophoresis. The released VeraTags were normalized to sample buffer volume and tumor area to give units of relative fluorescence per square millimeter of tumor (RF/mm^2). A panel of cell line controls was assayed together with the samples and used for batch-to-bath normalization. The antibody pairs used for the different assays are described below. HER2-HER3 heterodimer VeraTag assay: the HER2-HER3 heterodimer was measured by the proximity-dependent release of a VeraTag reporter from an anti-HER3 mouse monoclonal antibody (mAb) B9A11 (Monogram Biosciences) paired with an anti-HER2 rabbit mAb 29D8 (Cell Signaling Technology) and a biotinylated goat $F(ab')_2$ anti-rabbit IgG secondary antibody (Southern Biotech). HER3-phosphoinositide 3-kinase (HER3-PI3K) complex VeraTag assay: the HER3-PI3K complex was measured by the proximity-dependent release of a VeraTag reporter from anti-PI3 kinase, p85, N-SH3, mouse mAb AB6 (Millipore) paired with biotinylated anti-HER3 mouse mAb B9A11 (Monogram Biosciences).

Phosphorylated Protein Measurement

Mice bearing JIMT-1 tumor xenografts (100-150 mm^3) were treated with 2 or 4 weekly doses of antibody (25 mg/kg) or vehicle (PBS). 24 hr after the last dose, tumors were removed, flash frozen and processed to powder. Tumor lysates were prepared to a concentration of 50 mg tumor/ml by adding cold BioRad Lysis Buffer (supplemented with 0.4% BioRad Factor 1, 0.2% BioRad Factor 2, and 2 mM PMSF) to the frozen powder samples. Samples were then incubated at 4°C on a rocker for 60 minutes to ensure complete lysis. The samples were centrifuged at 4°C for 10 minutes at 16,000 x g and aliquoted. Total protein was determined using the Biorad DC Protein Assay reagents according to the manufacturer's instructions. Total Akt, phospho Akt Ser473 and Thr308 were detected using commercial Luminex kits (Millipore 48-618MAG and 46-645MAG) for each sample in duplicate. Dilutions were prepared in sample diluent to load approximately 25 μg protein per well for all total and phosphorylated analyte determinations. The Millipore kits were used according to the manufacturer's specifications.

Epitope Mapping

Alanine scanning mutagenesis was used to map the epitopes of anti-HER2 mAb PG3958 and anti-HER3 mAb PG3178. Clones were generated by substituting each amino acid residue of the HER2/HER3 ECDs with alanine (native alanines were substituted with serine). DNA of each clone was transfected into HEK293T cells. 24 hours later, the reactivity of antibodies was measured by immunofluorescent staining leading to binding maps and identification of critical residues for antibody binding. In parallel, expression levels of the HER2 and HER3 ECD constructs were verified by FACS analysis using commercially available monoclonal antibodies (R&D Systems, Cat#1129 (HER2) and Cat#66223 (HER3)). Binding of the antibodies was tested at a concentration of 0.25 μg/ml. The critical residues involved in binding were confirmed by introducing the specific point mutations into the HER2 or HER3 ECD constructs prior to FACS binding. Residues with >80% control antibody binding and <35% Fab binding were considered critical residues, nearby residues with decreased binding were considered "secondary" critical residues.

X-ray Crystallography

For crystallography studies, HER2 and HER3 ECDs were cloned upstream of a C-terminal histidine tag (6x) and produced in GnTI-deficient HEK293-EBNA cells (U-Protein Express), which yield shorter and more homogenous N-linked glycan chains suitable for crystallization of glycosylated proteins. Fab regions MF3958 and MF3178 were expressed in Freestyle™ 293-F cells (Invitrogen). His-tagged proteins were purified by IMAC column followed by gel filtration (Superdex 200 16/600), whereas the Fabs were purified by Capto-L affinity resin (GE Healthcare) followed by gel filtration (Superdex 75 16/600). Purified HER2 was mixed with MF3958 and purified HER3 with MF3178, in a 1:2 receptor:Fab ratio, and incubated overnight at 4°C. The complexes were separated from the excess of Fab by size-exclusion chromatography on a Superdex 200 10/30 column equilibrated with buffer containing 25 mM Tris pH 7.5 and 150 mM NaCl. The purified complexes were concentrated to 10 mg/ml. Crystals of the HER2-ECD:MF3958 complex were grown by hanging drop vapor diffusion technique, equilibrating the protein mixture with a reservoir solution containing 0.1 M MES pH 6.0 and 15% w/v PEG 6,000 in a 1:1 protein:mother liquor ratio at 18°C. Crystals of the HER3-ECD:MF3178 complex were grown at 18°C by sitting drop vapor diffusion, equilibrated in a 1:1 ratio with reservoir solutions containing 0.1 M Bis-Tris propane pH 8.5, 0.2 M KSCN and 20% w/v PEG 3350 (3.4 Å dataset), or 0.1 M Bis-Tris propane pH 7.5, 0.15 M sodium citrate and 20% w/v PEG 3350 (4.5 Å dataset). The crystals were transferred to cryo-protectant solutions with mother liquor and 20% v/v glycerol

(HER2:MF3958) or 25% v/v ethylene glycol (HER3:MF3178) and flash frozen in liquid nitrogen. Data for HER2-ECD:MF3958 was collected at the Swiss Light Source (SLS) and for HER3-ECD:MF3178 at the European Synchrotron Radiation Facility (ESRF). Diffraction data were integrated by IMOSFLM (Battye et al., 2011) and scaled and merged using the AIMLESS pipeline (Evans and Murshudov, 2013). The structures were solved by molecular replacement (MR) using PHASER MR (McCoy et al., 2007). For the MR of HER2-ECD:MF3958, the extracellular domain of rat HER2 (PDB: 1N8Y) was used as a first search model; in a second MR cycle, the LC from the Fab with PDB ID code 3SKJ and the HC from Fab with PDB ID code 2EH7 were used due to their high sequence homology. For the MR of HER3-ECD:MF3178 at 3.4 Å, iterative cycles were required using single domains of the extracellular portion of human HER3 (PDB: 1M6B), followed by the LC of the Fab with PDB ID code 3SKJ and the HC of the Fab with PDB ID code 4HCR. For the MR of HER3-ECD:MF3178 at 4.5 Å, iterative cycles using single domains of HER3-ECD were performed as described for the dataset at 3.4 Å, followed by the MF3178 Fab from the 3.4 Å structure. Iterative manual model building and refinement were carried out using COOT (Emsley et al., 2010) and PHENIX (Adams et al., 2010). The structures in the figures were generated by PyMOL version 1.5.0 (http://pymol.org).

SAXS

The SAXS data were collected at the European Synchrotron Radiation Facility (ESRF) using a BioSAXS beamline at 12.5 keV (0.9919 Å) with a 2D Pilatus 1M detector (DECTRIS). PB4188 was mixed with HER2 and HER3 ECDs in a 1:1:1 ratio and incubated overnight at 4°C. For online size-exclusion chromatography (SEC) the protein sample was automatically injected onto a Superdex 200 5/150 analytical column previously equilibrated with buffer containing 25 mM Tris pH 7.5 and 150 mM NaCl connected to an HPLC system (Shimadzu). Data were collected using a sample-to-detector distance of 2.81 m corresponding to a scattering vector s ($s=4\pi\sin\theta/\lambda$) range of 0.03 – 5.0 nm^{-1}. Approximately 1,500 frames were collected per 30 minutes sample run (1 frame per second). Data was processed automatically using EDNA pipeline, generating azimuthally integrated, calibrated and normalized one-dimensional profiles for each frame. Frames with a consistent radius of gyration (*Rg*) and corresponding to the highest protein concentration based on *I(0)* values were merged to yield a single averaged frame corresponding to the scattering of an individual SEC purified species (Figure S8A). The data was further processed using PRIMUS (Konarev et al., 2003) of the ATSAS suite. Radius of gyration (*Rg*) was evaluated within the range of Guinier approximation $sRg<1.3$ according to the equation $I(s) = I(0)e^{-\frac{(sRg)^2}{3}}$ (Figure S8B and Table S8). The *Rg* was also computed from the entire scattering pattern using Porod's law by the calculation of the paired distance distribution function *P(r)* using GNOM (Svergun, 1992) which gave also the maximum particle dimension *Dmax* (Figure S8C and Table S8). Kratky plot was calculated to judge the state of folding of the complex. The bell-shaped curve is consistent with compact, well-folded proteins (Figure S8D). A set of 20 low resolution *ab initio* models was generated using DAMMIF (Franke and Svergun, 2009).

QUANTIFICATION AND STATISTICAL ANALYSIS

All statistical tests were performed using Prism Software v6.0 (GraphPad). Where indicated, comparison between two groups was performed by two-tailed unpaired Student's t-test. For all experiments * is $p < 0.05$, ** is $p < 0.01$, *** is $p < 0.001$ and **** is $p < 0.0005$. Survival was analyzed using the Kaplan-Meier method and Log-rank (Mantel-Cox) test. In Figure 5F, $p < 0.017$ was considered statistically significant to correct for multiple comparisons (Bonferroni test).

DATA AND SOFTWARE AVAILABILITY

The HER2-ECD:MF3958 structure has been deposited in the Protein Data Bank (PDB) under ID code 5O4G. The HER3-ECD:MF3178 structures have been deposited in the PDB under ID codes 5O4O and 5O7P.